

5. SITE 787¹

Shipboard Scientific Party²

HOLE 787A

Date occupied: 23 April 1989
Date departed: 24 April 1989
Time on hole: 18 hr, 45 min
Position: 32°22.50'N, 140°44.64'E
Bottom felt (rig floor; m, drill pipe measurement): 3265.0
Distance between rig floor and sea level (m): 10.50
Water depth (drill pipe measurement from sea level, m): 3254.5
Total depth (rig floor; m): 3299.50
Penetration (m): 34.50
Number of wash cores (including cores with no recovery): 1
Total length of washed section (m): 34.50
Total core recovered (m): 6.00
Core recovery (%): 17
Oldest sediment cored:
Depth (mbsf): 34.50
Nature: scoriaceous and pumiceous sand and gravel
Age: late Miocene

HOLE 787B

Date occupied: 24 April 1989
Date departed: 27 April 1989
Time on hole: 2 days, 21 hr
Position: 32°22.50'N, 140°44.64'E
Bottom felt (rig floor; m, drill pipe measurement): 3269.4
Distance between rig floor and sea level (m): 10.50
Water depth (drill pipe measurement from sea level, m): 3258.9
Total depth (rig floor; m): 3589.5
Penetration (m): 320.10
Number of cores (including cores with no recovery): 34
Total length of cored section (m): 320.10
Total core recovered (m): 159.89
Core recovery (%): 50
Oldest sediment cored:
Depth (mbsf): 320.10
Nature: nannofossil-rich silty claystone and nannofossil claystone
Age: late Oligocene
Measured velocity (km/s): 2.25

Principal results: Site 787 is located on the eastern edge of the Izu-Bonin forearc sedimentary basin, about 95 km east of the arc volcano Aoga Shima and 135 km west of the axis of the Izu-Bonin

Trench. It is located in the axis of Aoga Shima Canyon; the canyon has incised and removed up to 1 km of the sedimentary section. The principal objectives of this site were to determine:

1. the stratigraphy of the forearc basin, which would help us understand temporal variations in sedimentation, depositional environment, and paleoceanography, and the history of intensity and chemistry of arc volcanism;
2. the uplift and subsidence history across the forearc, which would provide information on forearc flexure and basin development, as well as on the extent of any vertical tectonic activity that may have taken place following the formation of the forearc terrane; and
3. the post-Eocene microstructural deformation and large-scale rotation and translation of the forearc terrane.

The site was selected on the basis of multichannel seismic records and a short shipboard seismic survey, and lies on *Fred Moore* 3505, Line 2, at 0710Z. Site 787 was occupied from 1110Z on 24 April to 0300Z on 27 April 1989.

Hole 787A was spudded for rotary core barrel (RCB) operations at 0400Z on 24 April 1989. We washed 34.5 m below sea floor (mbsf) and recovered 6 m during the jet-in test. We continued RCB operations at Hole 787B, which cored 320.1 mbsf and recovered 50.0% (recovery was 73% from 127 to 282 mbsf). This hole penetrated the first strong seismic reflector before the pipe became stuck (probably a result of hole collapse) and eventually had to be severed with explosives 10 m below the mud line. Operations in Hole 787B ended at 0300Z on 27 April.

We defined four lithostratigraphic units at Site 787:

1. Unit I (0–21.4 mbsf): Quaternary sandy gravel, gravelly sand, gravel, and silty sand, all scoriaceous and pumiceous.
2. Unit II (21.4–40.3 mbsf): lower Pliocene and upper Miocene interbedded nannofossil ooze, nannofossil-rich silty clay, and nannofossil-rich clay.
3. Unit III (40.3–118.9 mbsf): upper Oligocene nannofossil-rich claystone, vitric silty claystone, claystone, and nannofossil chalk, with a lower 2.6-m-thick welded crystal-lithic lapilli tuff.
4. Subunit IVA (118.9–281.7 mbsf): upper Oligocene graded, sharp-based beds of sandstone, siltstone, and silty sandstone interbedded with bioturbated vitric silty claystone, nannofossil-rich silty claystone, and nannofossil-rich claystone; Subunit IVB (281.7–320.1 mbsf): upper Oligocene granule-rich and pebble-rich sandstone, silty claystone, silty sandstone, nannofossil chalk, and pebble conglomerate.

We dated Units I and II by means of nannofossil, foraminifer, and radiolarian biostratigraphy. Units III and IV are well dated by nannofossil biochronology and magnetostratigraphy (Chronos 6CN–9R). Sedimentation rates in the upper Oligocene range from 120 m/m.y. (at 29 Ma) to 33 m/m.y. (at 24 Ma).

Units I and II are unconsolidated, whereas Units III and IV are lithified. All sediments consist of mixtures of volcanogenic and biogenic (mainly nannofossil) materials that were deposited in water depths below 2000 m and above the carbonate compensation depth (CCD). Smectite is the dominant clay mineral in Units III and IV.

The volcanoclastic sands and gravels of Unit I represent Quaternary canyon fill. Unconformities form the upper and lower boundaries of Unit II, as well as internal separations within the unit. Unit II records intermittent hemipelagic deposition during canyon erosion. The lithification of the Oligocene section requires significant former overburden; we infer that canyon formation did not remove this overburden until the (probably late) Miocene or Pliocene.

¹ Taylor, B., Fujioka, K., et al., 1990. *Proc. ODP, Init. Repts.*, 126: College Station, TX (Ocean Drilling Program).

² Shipboard Scientific Party is as given in the list of participants preceding the contents.

The clastic component in Unit III results from distal turbidite deposition and volcanic ashfall, as well as one andesitic submarine pyroclastic flow. Subunit IVA represents basin-plain volcanoclastic turbidite deposits interbedded with fine-grained hemipelagic sediments. The biogenic component of the hemipelagic sediments decreases upward. Subunit IVB is probably a channel deposit, although the seismic data show evidence that this higher velocity coarse material is regionally distributed. All bedding is horizontal, except near a syndepositional slump unit at 189–195 mbsf that is 75% overturned. The upper Oligocene section is strongly burrowed. Extensional microfaults, conjugate fracture sets, low-angle shear planes, clastic injections, and dewatering veinlets all indicate extensional deformation.

Physical property measurements indicate that (1) carbonate content reaches a maximum in Unit III and varies inversely with clastic dilution from 0%–65%; (2) average bulk densities increase downward from 1700 to 2200 g/cm³; (3) sonic velocities average 1.8 km/s in Unit III and 2.2 km/s in Unit IV, with the exception of some thin coarse layers in these units that have velocities from 2.7 to 3.5 km/s; and (4) magnetic susceptibility is at a maximum in Units I and IV and at a minimum in Unit III. Magnetic inclination data cluster around $\pm 40^\circ$, which indicates 8° of northward motion since the late Oligocene.

Analyses of sediment and fluid geochemistry indicate that the interstitial waters are of marine origin and are modified by low-temperature alteration of volcanogenic material in the sediments. Reversal of K, Ca, and Mg concentration trends below 275 mbsf may be interpreted as the result of seawater circulation in a deeper layer. Uniformly high concentrations of sulfate, along with hydrocarbon gas levels below detection limits, are evidence of very low bacterial activity. The concentration of sedimentary organic carbon varies from 0% to 0.54%.

The principal results of this site are (1) characterization of late Oligocene hemipelagic and turbidite deposition in this deep-water forearc basin; (2) documentation of arc volcanism associated with moderate to high sedimentation rates in the late Oligocene, and extrapolation of average rates greater than 500 m/m.y. back to the presumed mid-Oligocene base of the forearc sediments (see "Site 792" and "Site 793" chapters, this volume); (3) paleomagnetic evidence that this site was translated about 8° to the north during the Neogene; (4) microstructural evidence of extensional deformation; (5) constraints on the time of major submarine canyon formation in this area to the (probably late) Miocene-Pliocene; and (6) pore-water indications of a possible seawater aquifer within the basin.

BACKGROUND AND OBJECTIVES

Site 787 is located at $32^\circ 22.50' N$, $140^\circ 44.64' E$, at 3259 mbsl (meters below sea level) on the eastern edge of the Izu-Bonin forearc sedimentary basin, about 95 km east of the arc volcano Aoga Shima ("Blue Island") and 135 km west of the axis of the Izu-Bonin Trench (Fig. 1). It is located in the axis of Aoga Shima Canyon (Fig. 2); the canyon has incised and removed up to 1000 m of the sedimentary section. Beneath the site, forearc-basin turbidites (>3 km total thickness) lap onto the western edge of the outer-arc basement high of presumed middle Eocene age (Fig. 3).

This first site of Leg 126 continued the drilling transect of the Izu-Bonin forearc region that was begun on Leg 125. The purpose of this program was to study the history of the Izu-Bonin forearc and to compare results of drilling in the Izu-Bonin forearc region with that accomplished in the Mariana forearc region by Deep Sea Drilling Project (DSDP) Leg 60 (Hussong, Uyeda, et al., 1982). By drilling in the forearc we sought to determine the following:

1. The stratigraphy of the forearc, and thus the temporal variations in sedimentation, depositional environment and paleoceanography, and the history of the intensity and chemistry of arc volcanism.
2. The uplift and subsidence history across the forearc, which would provide information on forearc flexure and basin development, as well as on the extent of any tectonic erosion.

3. The nature of the forearc igneous basement, which would resolve uncertainties concerning the nature of volcanism in the initial stages of subduction, the origin of boninites, and the formation of the 200-km-wide arc-type forearc crust.

4. The post-Eocene microstructural deformation and large-scale rotation and translation of the forearc terrane.

The first of these objectives was addressed partly through detailed studies of sediments retrieved at Site 787. The type of sedimentation and style of deposition in the forearc basin was expected to change with time as (1) the provenance changed from combined arc and outer-arc high to solely arc-derived, (2) the basin filled, (3) the volume and eruptive style of arc products varied, and (4) the development of submarine canyons eroded and redistributed sedimentary material. Geostrophic currents (e.g., the paleo-Kuroshio) and changes in global sea level may also have affected the pattern of sedimentation; these effects may be deciphered from the stratigraphic record.

The forearc sediments also contain a temporal record of the variations in the intensity and composition of arc volcanism. Studies of the chronology and geochemistry of tephra deposits at this site tested various conflicting models concerning the complex relationships between tectonic and volcanic phenomena in island arcs, such as changes in subduction rate, periodicity in backarc rifting and spreading, pulses of arc volcanism, and variations in arc geochemistry (see "Introduction" chapter, this volume, for elaboration).

The second objective was investigated through a combination of paleontological estimates of paleobathymetry, backstripping of the sedimentation history using the physical property and logging data, and seismic-stratigraphic analyses of interconnecting multichannel seismic (MCS) profiles. Determining the forearc vertical-displacement history provided some of the information necessary to decide whether (1) comparatively stable conditions have prevailed since the mid-Tertiary, as suggested by the well-developed submarine canyon system and lower-slope terrace of serpentinite seamounts; (2) the frontal arc and outer-arc high resulted from igneous construction or from differential uplift; (3) the upper-slope basin between them was formed by forearc spreading or differential subsidence; and (4) flexural loading of the forearc (either by arc volcanoes or by coupling with the subducting plate) is an important process.

The >80-m-thick Pleistocene pumice bed encountered at Site 785 limited penetration of the forearc-basin sedimentary section during Leg 125 (Fryer, Pearce, Stokking, et al., in press). Therefore, on Leg 126, we located Site 787 on the edge of the sedimentary basin (rather than at the initially proposed location on the edge of the outer-arc high) so that we could recover a sedimentary section representative of forearc-basin deposition. The site was drilled in a canyon axis so as to avoid a thick Pliocene-Pleistocene volcanoclastic sequence. However, the third objective of our forearc drilling (i.e., determining the nature of igneous basement) could not be addressed at this site because basement lies deeper than 2000 mbsf.

The fourth objective of the site, the study of microstructures and plate rotations, was addressed through a study of the structural and paleomagnetic properties of the cored materials. Microstructures in the drill cores indicate the intensity of faulting in space and time across the forearc terrane and define the syndepositional structures. Measurements of the paleomagnetic properties of subaerial portions of the Izu-Bonin and Mariana forearcs have shown at least 20° of northward drift, and from 30° to $>90^\circ$ of clockwise rotation since the Eocene (see "Introduction" chapter, this volume, for more details). Studies of the paleomagnetism of the cores constrained the numerous different models for the nature and timing of these motions, and their relationship to the overall structural evolution of the forearc.

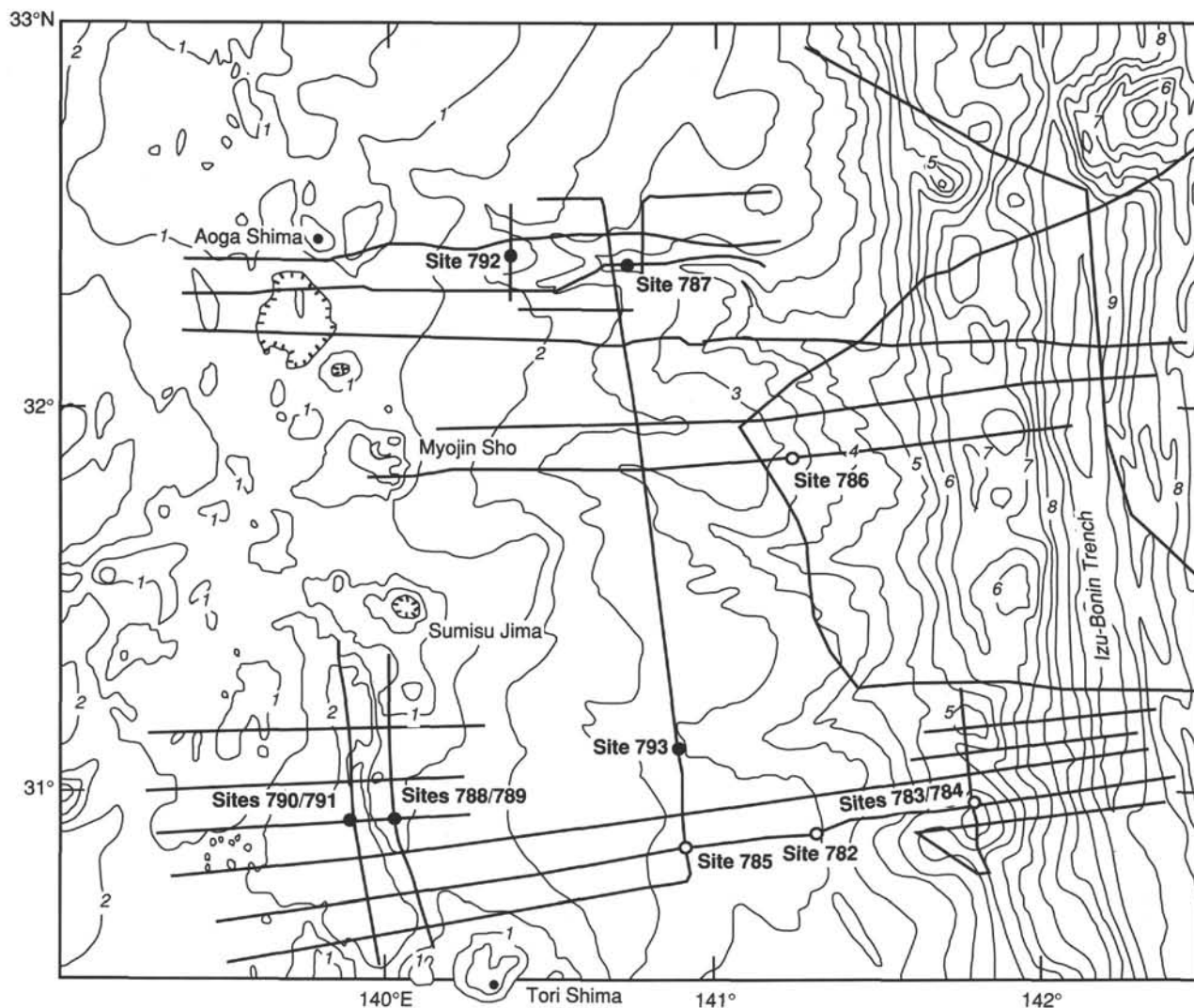


Figure 1. Bathymetric map of the Izu-Bonin arc-trench system between 30.5°N and 33°N. The locations of sites drilled on ODP Legs 125 (open circles) and 126 (solid circles) are shown on the map as are the locations of site survey multichannel seismic lines. Contour interval = 500 m (numbers on contour lines indicate depth in km).

SEISMIC STRATIGRAPHY

Correlation of site-survey MCS reflection data with recovered core material (Fig. 4) was accomplished by using the physical property velocity determinations, averaged over each lithologic unit (see "Physical Properties" section, this chapter), to convert sub-bottom depths (mbsf) into two-way traveltimes. The location chosen for Site 787 lies on *Fred Moore* 3505, Line 2, at 0710Z. The unconformity-bound Units I and II cannot be seismically characterized because they occur within the seismic bubble pulse. Low-amplitude, parallel, downlapping reflectors characterize Unit III and Subunit IVA. However, the automatic gain control (500-ms window) has lowered their amplitude with respect to the rest of the section as a result of the surrounding high-amplitude events associated with the seafloor and the coarse sand and gravel of Subunit IVB. Therefore, the entire seismic section at Site 787, from the bubble pulse to 5.36 s, is characterized by parallel, continuous, medium- to high-amplitude reflectors typical of basin-fill turbidites, with two extra-high-amplitude reflectors associated with the top and bottom of Subunit IVB. These reflectors lap onto a westward-dipping, high-amplitude sequence (5.36–5.77 s) that in turn laps onto the seismically chaotic acoustic basement.

OPERATIONS

Tokyo to Site 787

JOIDES Resolution departed Tokyo at 1700 hr (all times given in UTC) on 22 April 1989, and steamed toward Site 787 (proposed Site BON-5C). The first site was selected on the basis of our need to occupy the deepest-water site first; the new television (TV) coaxial cable had to be paid out to maximum depth and allowed to detorque prior to its first use in conjunction with the drill pipe. We selected proposed Site BON-5C and the ship proceeded directly to that site. The availability of either a global positioning satellite (GPS) window or adequate Loran navigation coverage would determine whether or not we performed the pre-site survey and dropped the beacon prior to the cable detouring exercise. As it turned out, GPS was unavailable but the Loran fixes appeared to be accurate, so we conducted the pre-site survey in a normal fashion (see "Underway Geophysics" chapter, this volume). One north-south pass was made over the site, followed by an east-west pass during which the beacon was dropped. One beacon, poised over the side and ready for release on command, broke free without weights and drifted away. A backup beacon was readied in just 6 min and released as the ship was about to leave the acceptable drop zone.

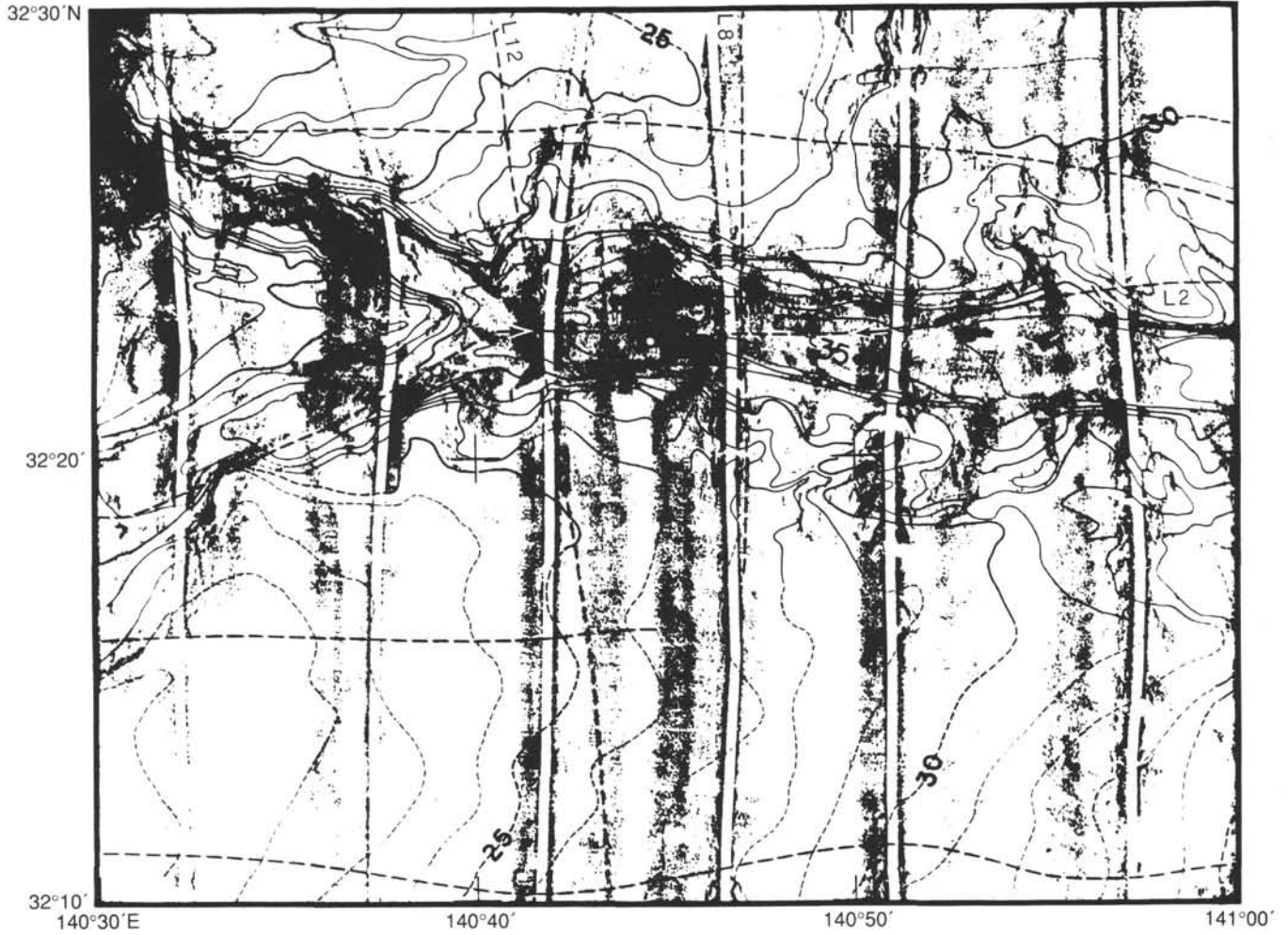


Figure 2. SeaMARC II sidescan and bathymetry (contour interval = 100 m) of Aoga Shima Canyon (Klaus and Taylor, in press). The locations of MCS site-survey tracks and of Site 787 (open circle) are also shown. The segment of MCS Line 2 shown in Figure 3 is delineated by arrows.

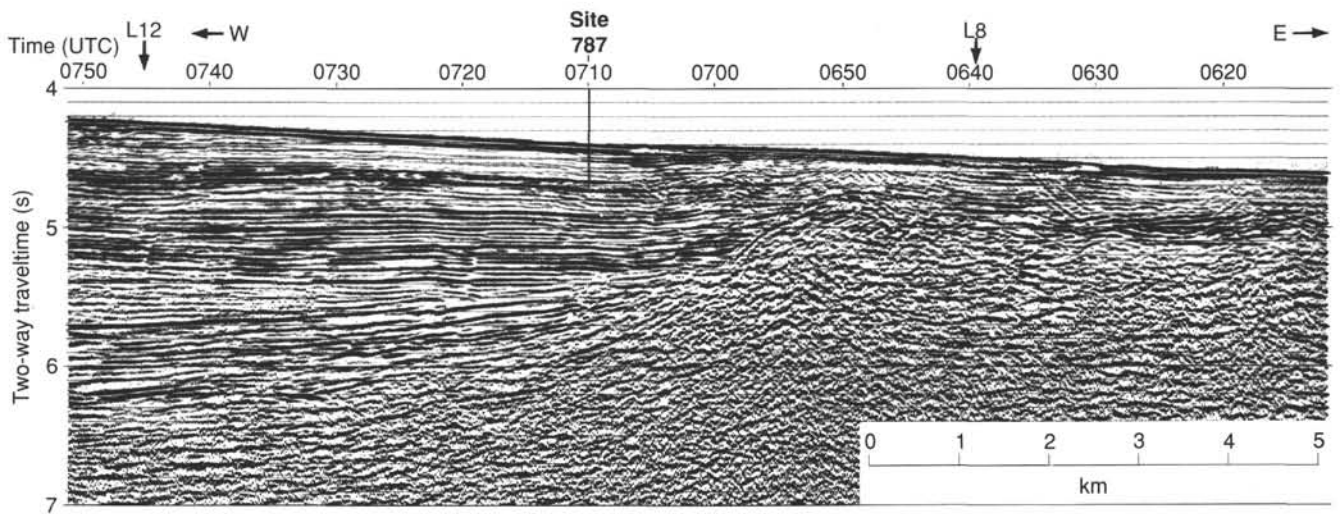


Figure 3. MCS Line 2 (Taylor et al., this volume) across the Izu-Bonin forearc sedimentary basin and outer-arc high. This profile was shot along the axis of Aoga Shima Canyon (see Fig. 2 for location). Site 787 is located on the eastern edge of the basin, where the deeper sedimentary section laps onto the outer-arc high.

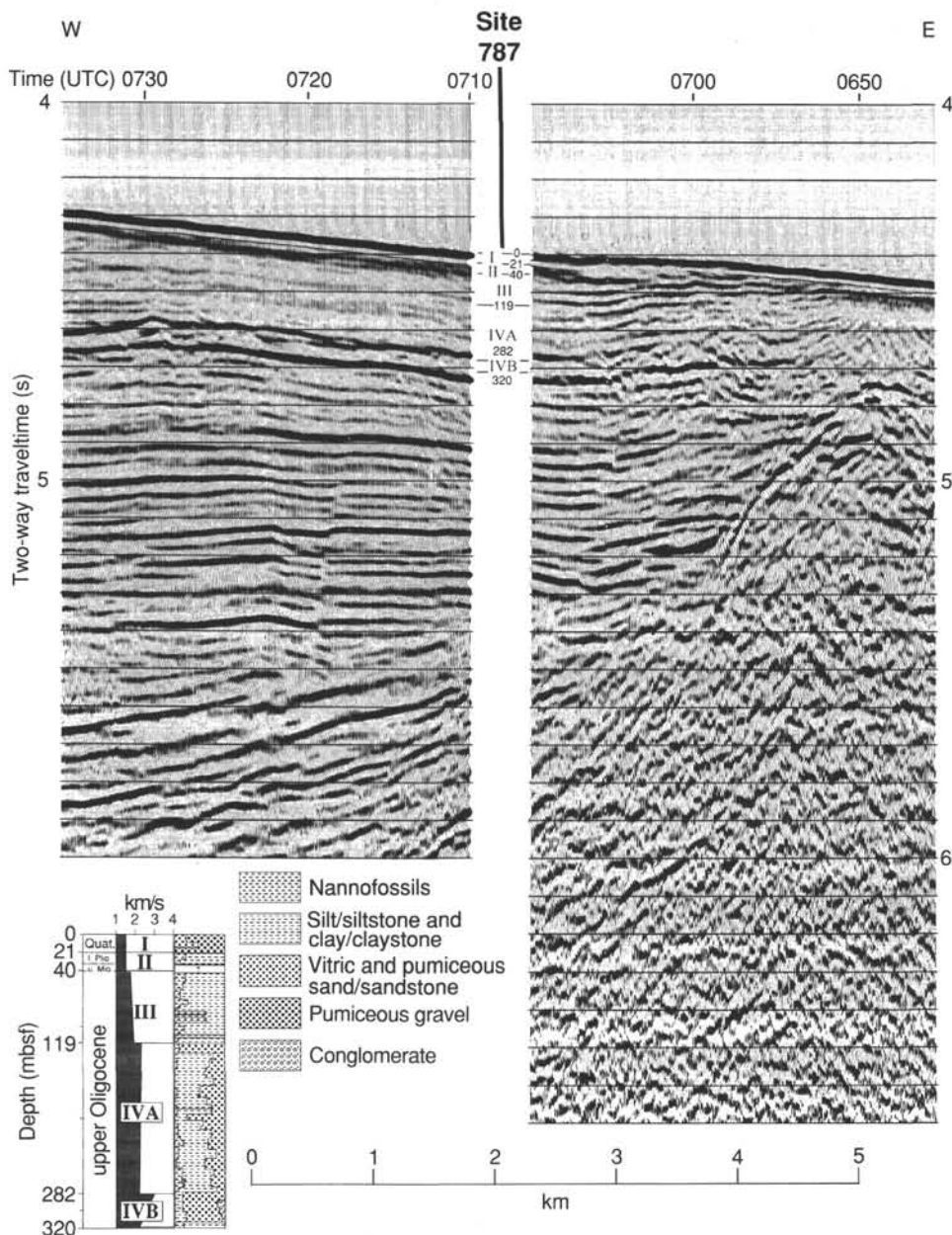


Figure 4. Correlation of Site 787 lithostratigraphy with site-survey multichannel seismic reflection data. Lithologic units are identified on the seismic section, unit boundaries are given in mbsf, and the lithologic column (see "Lithostratigraphy and Accumulation Rates," this chapter) is presented in the lower left corner. The location of the *Fred Moore* seismic line is shown in Figure 2. The seismic section has been stacked (48-fold), deconvolved, migrated, and filtered 10–60 Hz. Vertical exaggeration is about 4X.

Site 787

The second beacon was deployed at 1110 hr on 23 April, initiating Site 787. The seismic survey line was continued for 5 nmi before the gear was pulled. As the ship returned over the beacon and the thrusters were lowered, heavy seas dislodged several large portions of a reentry-cone assembly that were loose on the main deck. These steel brackets moved across the deck and landed partly on an exposed section of the TV coaxial cable that had been strung out in preparation for the detorquing run. The damage to the cable made its watertightness suspect, so the detorquing exercise was postponed.

Hole 787A

The potential target depth for the site was as deep as 1400 mbsf, which was expected to require more than one bit. One of the possible scenarios for operations at the site was the emplacement of a full reentry cone and installation of casing. Accordingly, Hole 787A was to be a jet-in test to determine the depth for jetting in 16-in. casing with a full-size reentry cone.

The anticipated seafloor conditions suggested lithified sediments at or near the surface, and interbedded volcanoclastic materials and claystones below. The RCB was deemed best for the type of formation expected, and a standard nine-drill-collar

bottom-hole assembly (BHA) with a hydraulic bit release (HBR) was assembled and run to the seafloor. The precision depth recorder (PDR) indicated a firm reflector at the seafloor in 3272.0 m of water.

The seafloor proved to be more suitable for jetting than anticipated. The hole was spudded at 0400 hr on 24 April, and the bit was successfully jetted in to a presumed sub-bottom depth of 34.5 mbsf, on the basis of apparent mud-line contact at 3254.5 mbsl. At that point, firmer material was encountered. The bit was pulled clear of the seafloor at 0555 hr, and we retrieved the core barrel used for the jet-in test. Unexpectedly, 6.00 m of pumiceous and scoriaceous gravel had been trapped in the core barrel. Scientific interest in the material was high, so the core was designated a wash core and the jet-in hole became Hole 787A.

Hole 787B

The ship was offset 20 m northeast, and Hole 787B was spudded at 0747 hr. Coring with the RCB in the unconsolidated sand and gravel at the seafloor was unexpectedly successful. The first three cores each recovered an average of 3.74 m of material, with circulation, pipe rotation, and weight on the bit all at a minimum (Table 1). The following five RCB cores were from an interval of apparently firm but loose sand or gravel in which

recovery was almost impossible. Only the more consolidated nanofossil-rich claystones were recovered. Despite this ominous start, the conditions for rotary coring improved dramatically at that point, and the next 22 cores (126-787B-9R to -30R) were very good in terms of the percentage and quality of core recovered. The formation contained just enough claystone and clay-bearing sedimentary material to stabilize the hole and, evidently, "make its own mud," thus preventing loose material near the surface from causing fill or pipe-sticking problems. We recovered several well-preserved rock/claystone contacts, which indicated unusually favorable conditions not typically encountered during RCB coring of interbedded lithologies.

The good drilling conditions ended abruptly after encountering an interval of unconsolidated coarse sandstone at 282 mbsf. The hole was deepened to 320.1 mbsf, with recovery averaging 2.2 m/core over the last four cores. The low recovery rate suggested a highly unstable zone, but hole conditions were quasi-stable until the sinker bars stabbed into the top-drive swivel to retrieve Core 126-787B-34R. At that point, severe backflow indicated the probability of hole collapse. After the sinker bars were in place and the wireline blowout preventer could be closed, we found the bit to be plugged. The core barrel was stuck briefly at the bit, suggesting flow-in of loose material around the core barrel at the bit. By the time we retrieved the core barrel to the deck, the pipe was firmly stuck. Although we regained circulation, we could not work the pipe free. After 3½ hr of continuous overpulls, we decided to sever the pipe and abandon the hole.

The first 31-pellet high-energy engineering (HEE) severing charge was fired in the 5½-in. transition joints at the top of the BHA, but the charge was a partial failure and the pipe did not come free. We fired the second charge 10 m below the mud line, as the first charge could have failed because it had been applied below the free point of the drill string. The second shot was successful, and the pipe came free with minimum pull. The pipe was then pulled, and the severed joint reached the deck at 0300 on 27 April.

LITHOSTRATIGRAPHY AND ACCUMULATION RATES

We recognized four lithologic units at Site 787 (Table 2, Fig. 5). The upper two units are unconsolidated, whereas the lower two are lithified. The contacts between Units I, II, and III were not recovered. All sediments at this site consist of mixtures of volcanogenic and biogenic materials (mainly nanofossils). Bedding in the entire section is essentially horizontal, except immediately above a slide unit in Core 126-787B-21R. Minor deformation and dewatering features include subvertical veinlets, extensional microfaults, low-angle shear planes, and clastic injections.

Figure 5 also shows downhole distribution of carbonate minerals (mainly nanofossil tests) and trends in magnetic susceptibility. In many cases, peaks in magnetic susceptibility correspond to concentrations of magnetic minerals and mafic volcanic glass, particularly in fine-grained sediments that contain bioturbation-disseminated ash.

Unit I

Interval: Cores 126-787B-1R through -3R

Age: Quaternary

Depth: 0–21.4 mbsf

Unit I (0–21.4 mbsf) consists mainly of sandy gravel (49%), gravelly sand (28%), gravel (11%), and silty sand (9%), all scoriaceous and pumiceous; recovery averaged 52%. We interpret the complete lack of primary structures and the occurrence of coarsest material in the lower part of each core to be the result of drilling disturbance.

Table 1. Coring summary, Site 787.

Core no.	Date (April 1989)	Time (UTC)	Depth (mbsf)	Cored (m)	Recovered (m)	Recovery (%)
126-787A-						
1W	24	0710	0.0	34.5	6.00	17
Coring totals				0.0	0.00	
Washing totals				34.5	6.00	
Combined totals				34.5	6.00	
126-787B-						
1R	24	0830	0.0–2.3	2.3	2.32	101.0
2R	24	1025	2.3–11.9	9.6	5.29	55.1
3R	24	1145	11.9–21.4	9.5	3.61	38.0
4R	24	1300	21.4–30.9	9.5	0.46	4.8
5R	24	1420	30.9–40.3	9.4	0.39	4.2
6R	24	1525	40.3–49.8	9.5	2.20	23.1
7R	24	1700	49.8–59.3	9.5	1.80	18.9
8R	24	1800	59.3–69.0	9.7	0.57	5.9
9R	24	1900	69.0–78.7	9.7	3.48	35.9
10R	24	2020	78.7–88.4	9.7	3.86	39.8
11R	24	2145	88.4–98.1	9.7	3.38	34.8
12R	24	2335	98.1–107.8	9.7	2.49	25.7
13R	25	0135	107.8–117.5	9.7	3.78	38.9
14R	25	0400	117.5–127.2	9.7	4.22	43.5
15R	25	0555	127.2–136.8	9.6	6.76	70.4
16R	25	0730	136.8–146.5	9.7	6.43	66.3
17R	25	0900	146.5–156.2	9.7	7.46	76.9
18R	25	1040	156.2–165.8	9.6	4.27	44.5
19R	25	1215	165.8–175.5	9.7	9.46	97.5
20R	25	1340	175.5–185.1	9.6	5.82	60.6
21R	25	1500	185.1–194.8	9.7	9.82	101.0
22R	25	1620	194.8–204.4	9.6	0.98	10.2
23R	25	1745	204.4–214.1	9.7	7.69	79.3
24R	25	1855	214.1–223.7	9.6	9.78	102.0
25R	25	2010	223.7–233.4	9.7	8.22	84.7
26R	25	2130	233.4–243.0	9.6	7.68	80.0
27R	25	2240	243.0–252.7	9.7	5.32	54.8
28R	25	2350	252.7–262.4	9.7	8.01	82.6
29R	26	0100	262.4–272.0	9.6	7.62	79.4
30R	26	0215	272.0–281.7	9.7	7.68	79.2
31R	26	0340	281.7–291.3	9.6	1.87	19.5
32R	26	0500	291.3–300.8	9.5	2.60	27.3
33R	26	0645	300.8–310.5	9.7	2.68	27.6
34R	26	0815	310.5–320.1	9.6	1.89	19.7
Coring totals				320.1	159.89	50.0

Table 2. Lithostratigraphic units, Hole 787B.

Unit	Lithology	Sedimentary structures	Interval (mbsf)	Age	Occurrence
I	Pumiceous and scoriaceous sandy gravel, gravelly sand, gravel, and silty sand.	Cores all show upward fining owing to drilling disturbance. No primary structures noted. Maximum clast size is 3 cm.	0-21.4	Quaternary	126-787B-1R to -3R
II	Interbedded nannofossil ooze, nannofossil-rich silty clay, and nannofossil-rich clay.	None observed (poor recovery).	21.4-40.3	early Pliocene to late Miocene	126-787B-4R and 126-787B-5R
III	Nannofossil-rich claystone, vitric silty and sandy claystone, claystone, and nannofossil chalk. Cores 126-787B-12R and -13R contain a welded crystal-lithic lapilli tuff.	Sediment contains disseminated ash and is bioturbated; burrows include <i>Zoophycos</i> , <i>Planolites</i> , and <i>Chondrites</i> . Common dewatering veinlets, clastic dikes, and microfaults.	40.3-118.9	late Oligocene	126-787B-6R to -14R-1, 135 cm
IVA	Graded, sharp-based, parallel- to ripple-laminated beds of sandstone, siltstone, and silty sandstone interbedded with bioturbated vitric silty claystone, nannofossil-rich silty claystone, and nannofossil-rich claystone. Carbonate content increases downhole.	Fine-grained sediments contain local concentrations of sand-sized ash and are bioturbated; burrows include: <i>Zoophycos</i> , <i>Planolites</i> , and <i>Chondrites</i> . Silty sandstone beds have sharp bases, are graded, and show internal structures of the Bouma sequence (generally the parallel-laminated and rippled divisions). Injections and extensional microfaults characterize this subunit. Core 126-787B-21R contains two overturned intervals and slide folds.	118.9-281.7	late Oligocene	126-787B-14R-1, 135 cm, to -30R
IVB	Granule-rich and pebble-rich sandstone, silty claystone, silty sandstone, nannofossil chalk, and pebble conglomerate.	No primary structures in the sandstone; burrows and microfaults in the finer sediment.	281.7-320.1	late Oligocene	126-787B-31R to -34R

Maximum clast size in Unit I is approximately 3 cm. The major clast types are pumice (white, gray, rarely red) and black scoria (Fig. 6). Other grains include plagioclase, quartz, and minor bioclasts (benthic foraminifers, gastropods, and bryozoans).

Unit II

Interval: Cores 126-787B-4R and -5R
Age: early Pliocene to late Miocene
Depth: 21.4-40.3 mbsf

Unit II was sampled in only two, short, core sections (total recovery = 85 cm) and consists of lithic-vitric-rich nannofossil ooze (58%), nannofossil-rich volcanic-lithic silty clay (35%), and nannofossil-rich clay (7%). Total recovery was 4.5% of the cored interval. This material contains no primary structures other than bedding.

Unit III

Interval: Core 126-787B-6R through Section 126-787B-14R-1 at 135 cm
Age: late Oligocene
Depth: 40.3-118.9 mbsf

Unit III is dominated (60%) by nannofossil-bearing sediment types: nannofossil-rich claystone (38%), nannofossil chalk (19%), nannofossil vitric silty claystone (3%), and nannofossil claystone (1%). Noncalcareous sediments and rocks make up the remaining 40% of the unit: predominantly vitric silty and sandy claystone (18%), claystone (10%), and a 2.6-m-thick crystal-lithic lapilli tuff (13%). Some laminated claystones and minor graded bedding are present; however, most of the sediment in this unit is bioturbated. Trace fossils include *Zoophycos*, *Planolites*, and *Chondrites* (Figs. 7 and 8). Sand-size volcanic ash is commonly scattered throughout the burrowed sediment (Figs. 5 and 9). Total recovery was 29% of the cored interval.

Unit III, unlike the overlying Units I and II, is lithified and has been deformed by extension. Evidence of this deformation includes rotated (kinked), subvertical, mineral-filled veinlets with

braided and anastomosing geometries (Figs. 7 and 8), low-angle shear planes or zones (Fig. 7), and numerous microfaults (Fig. 10). The mineral-filled veinlets are identical to those described from the Middle America Trench slope by Ogawa and Miyata (1985) and from the Japan Trench by Arthur et al. (1980) and Lundberg and Leggett (1986); they are particularly common in Cores 126-787B-7R through -10R. The low-angle shear zones generally are planar bands of homogeneous claystone, a few millimeters thick, which offset primary structures. These zones are very subtle, and many may not have been recognized in dark-colored sections. The extensional stress field also may have helped promote the injection of clastic dikes, which are common in this unit (Fig. 11).

Near the base of Unit III, there is a 2.6-m-thick andesitic crystal-lithic lapilli tuff with welded texture (Fig. 12). The base of this unit is chilled and contains vesicles (Fig. 13); the top is overlain sharply by nannofossil-rich vitric silty claystone. Clasts consist of gray andesite, and clots of plagioclase and pyroxene crystals. In thin section (Sample 126-787B-13R-1, 27-30 cm), the welded lapilli tuff is formed mainly of andesitic clasts (2-4 mm in size) and crystal fragments (1 mm in size). The andesitic clasts are generally moderately porphyritic, with zoned plagioclase and clinopyroxene phenocrysts in a glassy groundmass. Locally, the feldspar microlites within these clasts are aligned.

The glassy groundmass found in Unit III is partly hydrated to brown palagonite, which contains a few feldspar microlites formed during devitrification; vesicles (<0.5 mm) are abundant and filled with zeolites and palagonite. A few clasts are formed of glomeroporphyritic plagioclase with small clinopyroxenes. The crystal fragments consist of complete or broken plagioclase and clinopyroxene. The plagioclase crystals show oscillatory zoning. Some of the clinopyroxene crystals are corroded and exhibit orthopyroxene lamellae inclusions that suggest a fairly slow cooling rate. The groundmass consists predominantly of clear, amorphous, volcanic glass or possibly amorphous silica and minor brown devitrified glass.

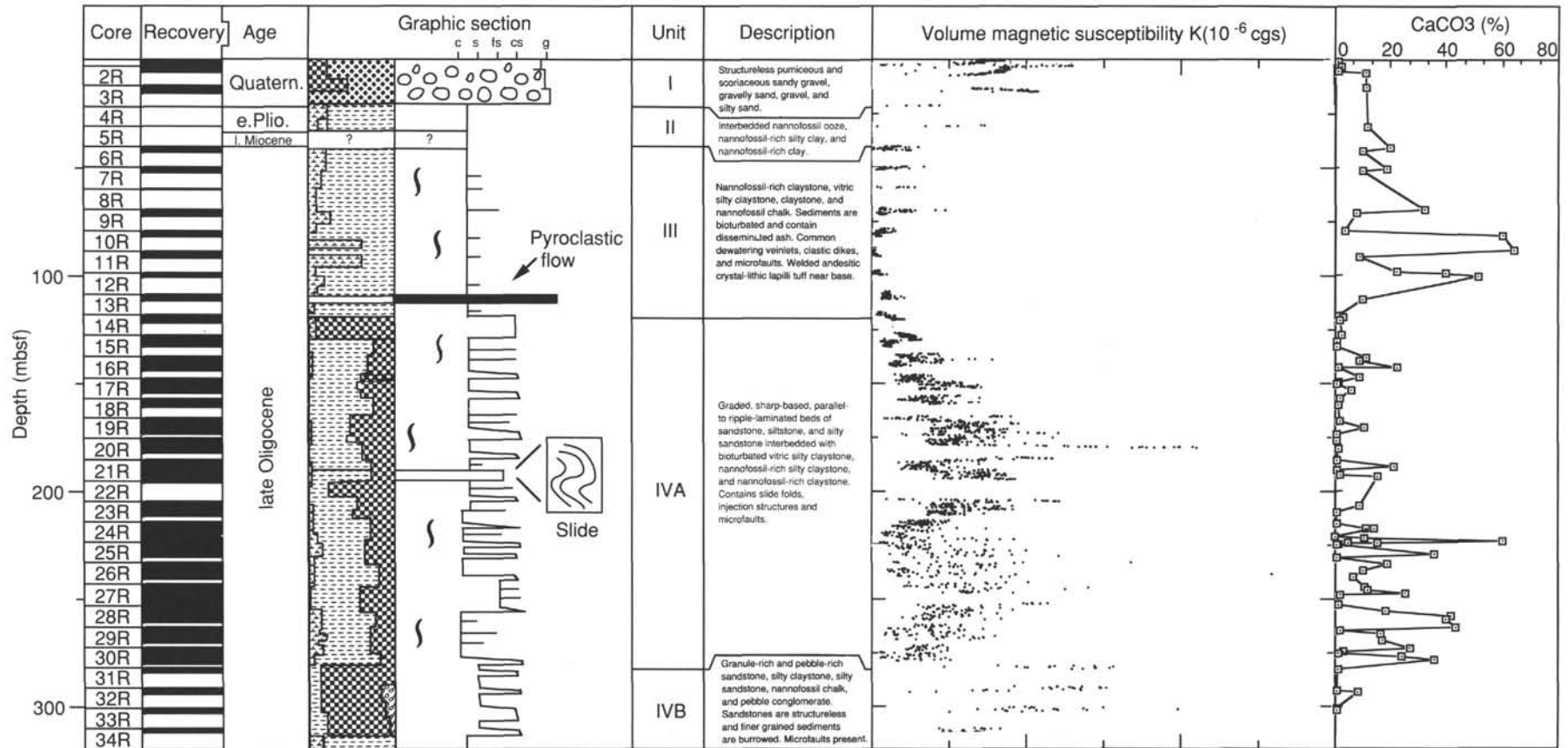


Figure 5. Lithostratigraphic summary for Site 787, including a graphic display of core recovery and the downhole distributions of carbonate minerals and magnetic susceptibility. The carbonate curve is primarily a function of nannofossil distribution throughout the section, whereas the magnetic susceptibility data reflect the distribution of coarse mafic volcanic lithic rocks and crystals. The proportions of sediment types at Hole 787B are shown in the lithology column (see Fig. 4 for key to patterns). The format is more generalized than in the core descriptions (which appear at the back of this volume), reflecting the percent of lithologic groups observed in the cored intervals (e.g., silt + clay, sand, gravel, carbonate), and does not show mixed biogenic/siliciclastic sediments. The graphic column is a simplified sedimentological log that displays relative grain size on the horizontal axis (c = clay/claystone, s = silt, fs = fine sand, cs = coarse sand and g = gravel/conglomerate). On this column, sedimentary structures (see Fig. 6, "Explanatory Notes" chapter, this volume) and bedding within the cored units are schematically displayed.

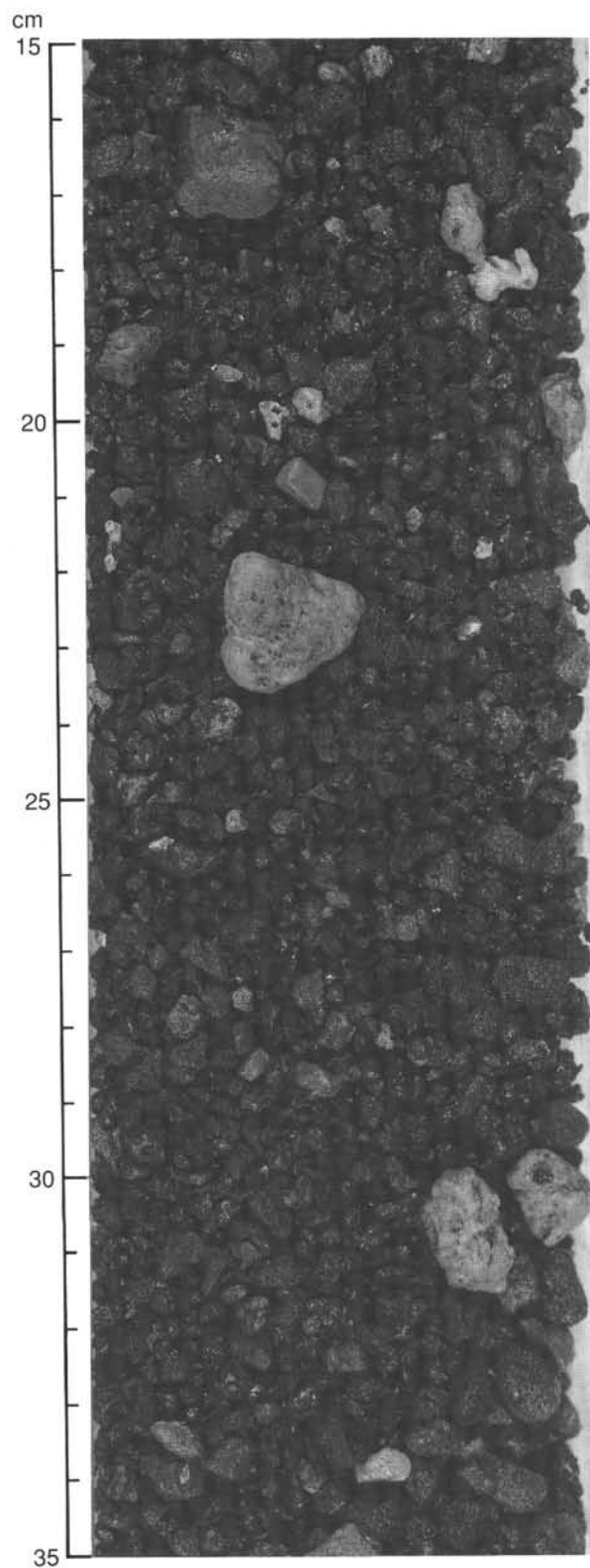


Figure 6. Dark, scoriaceous gravel of Unit I, with interspersed light gray pumice pebbles. Interval shown is 126-787B-1R-2, 15–35 cm.

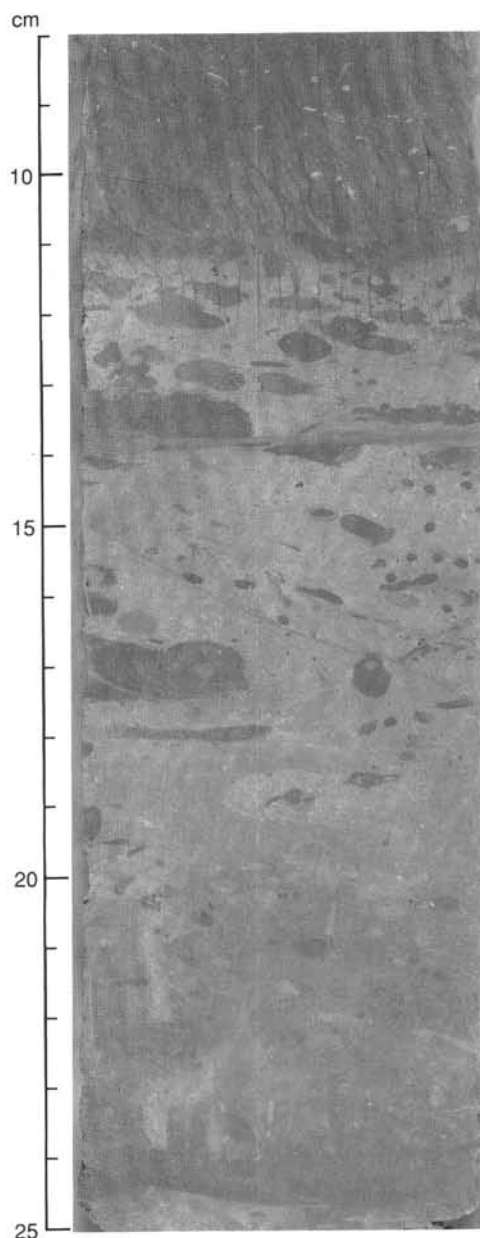


Figure 7. Heavily burrowed zone of nannofossil-rich claystone in Unit III (Interval 126-787B-9R-1, 8–25 cm). Note equidimensional and ovoid *Planolites* burrows that are 0.5–1.0 cm in diameter at 11–18 cm, and small *Chondrites* burrows at 14–16 cm. Microshears occur at 15–18 cm. A shear plane at 14 cm offsets burrows. The fine dark vertical streaks from 8 to 12 cm are veinlet structures formed during early dewatering.

Unit IV

Interval: Section 126-787B-14R-1 at 135 cm, through Core 126-787B-34R
 Age: late Oligocene
 Depth: 118.9–320.1 mbsf

Unit IV is divided into two subunits at 281.7 mbsf. Subunit IVA is the top of a sand-rich turbidite succession. Subunit IVB differs from Subunit IVA in that it contains several intervals of granule-rich coarse sandstone and pebbly sandstone. Recovery was 71% for Subunit IVA, and 24% for Subunit IVB. As in Unit III, all finer grained intervals are burrowed and contain variable amounts of disseminated sand- to silt-size volcanic ash

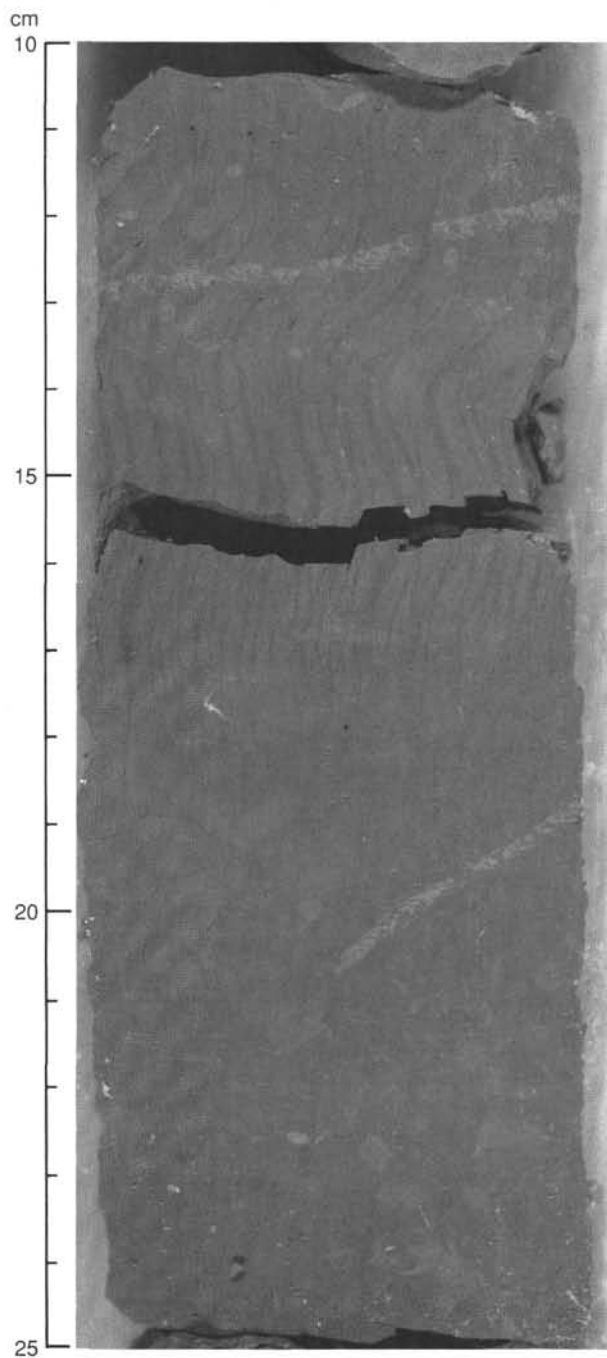


Figure 8. Indistinctly mottled claystone is crosscut by two simple *Zoophycos* burrows (12–13 and 19–20 cm). The upper burrow is deformed by closely spaced, wavy, vertical veinlet structures that extend across the interval from 11 to 17 cm. Interval shown is 126-787B-10R-1, 10–25 cm.

(Figs. 5 and 14). Volcanic ash is also commonly concentrated in discrete beds of brownish black, lithic-crystal-vitric siltstone and fine-grained sandstone (Fig. 15).

Subunit IVA is characterized by the intercalation of two sediment types. The first consists of dark-colored, thin- to thick-bedded, sharp-based, graded, vitric sandstones (23% of the total material recovered), vitric silty sandstone (15%), and vitric siltstone (6%) beds. The second sediment type consists of strongly burrowed claystones (11%), vitric silty claystones to clayey siltstones (7%), and nannofossil-bearing sediments (36%). The

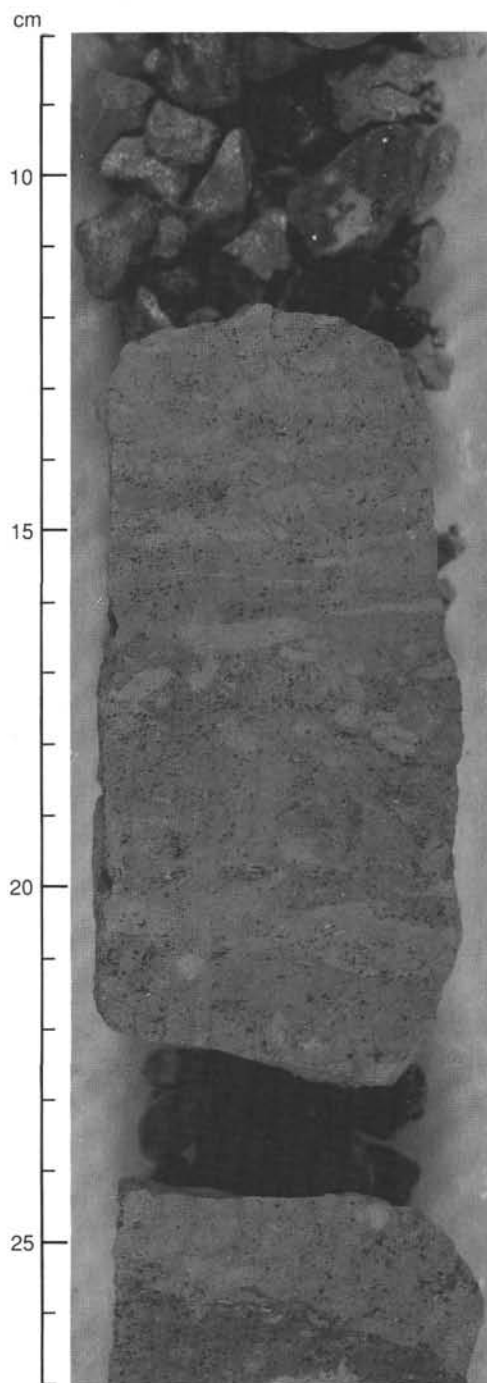


Figure 9. Black sand-size ash disseminated throughout a bioturbated nannofossil-rich claystone. Interval shown is 126-787B-8R-1, 8–27 cm.

burrows extend downward into the upper part of the graded silty sandstone and siltstone beds (Fig. 16), creating mixed nannofossil-bearing sediments: nannofossil-rich vitric silty claystone (19%), nannofossil-rich claystone (12%), nannofossil-rich siltstone (3%), and nannofossil claystone (2%). The quantity of biogenic carbonate (i.e., nannofossils) in the finer grained lithologies increases downward in Subunit IVA, and beds of nannofossil-rich claystone and nannofossil-rich silty claystone, etc., become common below Core 126-787B-22R (Fig. 5).

Internal structures in the graded silty sandstone and siltstone beds include parallel lamination, ripple lamination, rare convo-

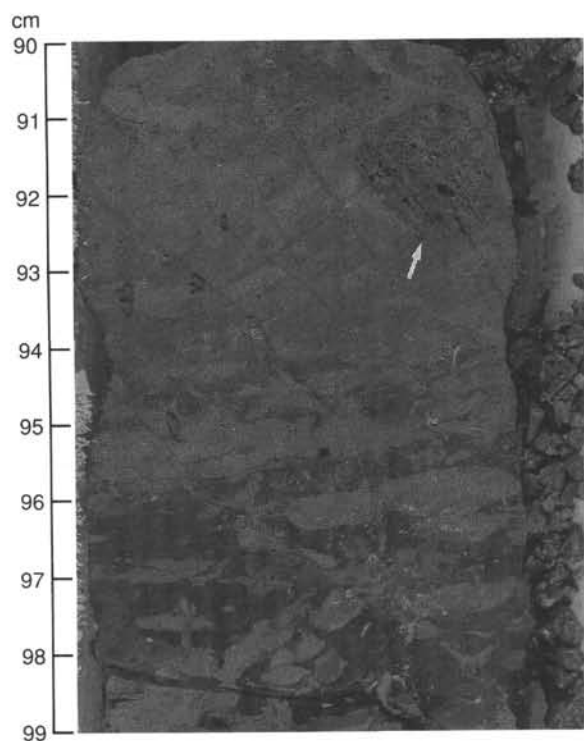


Figure 10. Microfractures with an apparent dip of 45° cutting bioturbated vitric-rich nanfossil chalk. Note 1.5-cm-diameter pumice pebble at 92 cm (indicated by arrow). Interval shown is 126-787B-7R-1, 90-99 cm.

lute lamination, and silt-mud laminae at the top. The sequences of structures are identical to those described for turbidites by Bouma (1962). Bases of the beds are almost always sharp, and in some cases have basal scour marks. Trace fossils include *Planolites*, *Zoophycos*, and *Chondrites*.

The sandstone percentage and the relative thickness of sandstone beds are greatest near the top of Subunit IVA. Below Core 126-787B-15R, graded silty sandstone and siltstone beds are thin, and burrowed claystone and nanfossil-rich claystone units are thick; some cores contain very little sand. In Cores 126-787B-19R and -20R, sandstone beds are comparatively thick (1-2 m maximum). In general, sandstone/siltstone bed thicknesses and the sandstone/shale ratio vary between cores, suggesting cyclicity in these parameters on a scale of tens of meters.

Core 126-787B-21R contains a deformed interval from Section 126-787B-21R-3 at 110 cm, to -21R-7 at 70 cm (thickness = 5.6 m). Approximately 75% of the sediment in this interval is overturned, and two horizons of sandy mudstone and clayey siltstone are plastically folded (Fig. 17). The deformed interval is accompanied by extensional microfaults (Fig. 18) and sandstone injections (Fig. 19). The overturned bedding is confirmed by a reversal in magnetic polarity in this interval (see "Paleomagnetism" section, this chapter). Immediately above this zone, the beds show as much as 20° of apparent dip, but they are horizontal well above and below the overturned sequence.

Smear-slide data show that the silty sandstones and siltstones are formed almost entirely of volcanic grains. The vitric/lithic/crystal ratios are variable. The vitric component consists of dark brown to clear glass shards and pumice fragments. Crystals are mainly plagioclase, with less abundant pyroxene and rare epidote. Volcanic lithic fragments are mainly microlitic in texture. Many beds are rich in black sand in their basal parts, particularly in the lower part of the subunit, and in smear slides

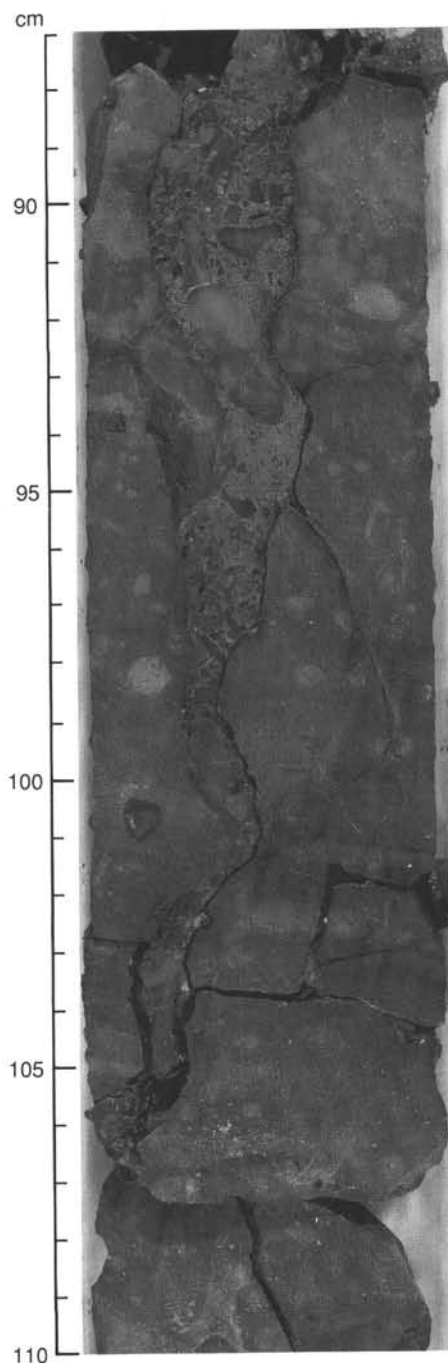


Figure 11. V-shaped, subvertical clastic dike crosscutting silty claystone. The dike consists of brecciated silty claystone clasts within a poorly sorted matrix. Interval shown is 126-787B-14R-1, 87-110 cm.

we observed this material to consist of dark glass and lithic grains.

Subunit IVA contains structural features that indicate brittle deformation under extension has taken place, predominantly microfaults that locally have conjugate fracture sets (Fig. 20). Healed fractures are visible in some cores.

Subunit IVB consists of granule-rich and pebbly sandstone (46%), silty claystone (20%), silty sandstone (14%), nanfossil chalk (11%), and pebble conglomerate (9%). The coarse sandstone and minor conglomerate are structureless and contain scattered large-pebble- and cobble-size claystone clasts that have

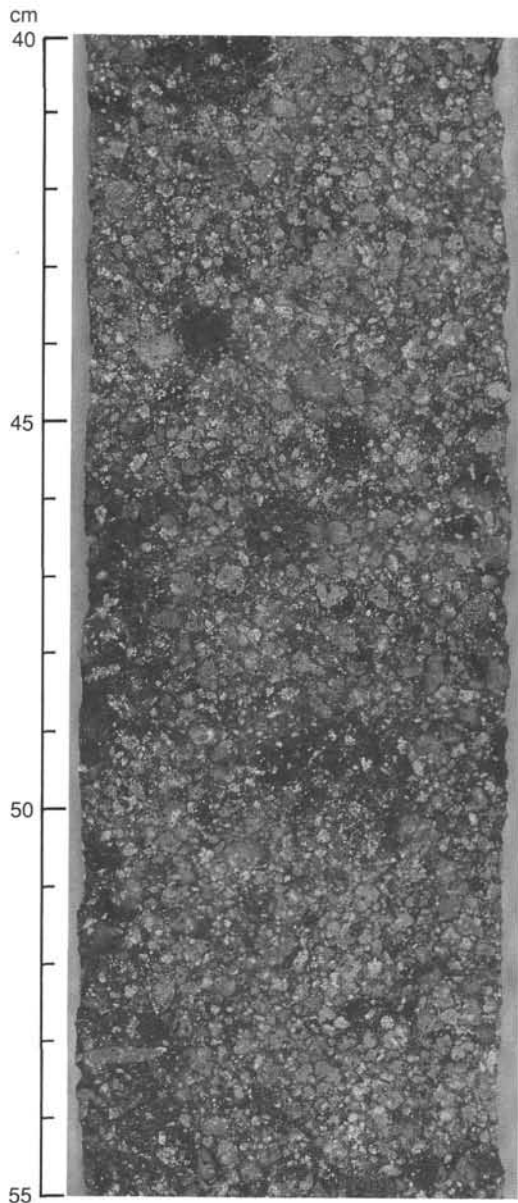


Figure 12. Welded lapilli tuff near the base of Unit III. Interval shown is 126-787B-13R-1, 40–55 cm.

the same composition and approximate age as the interbedded sediment, as determined from nannofossil dates. Pebbles, granules, and sand grains are composed of mafic and felsic volcanic lithic rocks, pumice, quartz, feldspar, and rare red pumice. Microfaults are present in the fine-grained units. Recovery in this subunit was relatively low, probably because the weakly cemented coarse sandstone tended to crumble; therefore, the percentage of fine-grained lithologies may be significantly lower than that calculated from recovered intervals.

X-Ray Diffraction Analysis

X-ray diffraction (XRD) results for Units I, III, and IV in Hole 787B are shown in Table 3. In Unit I, the clay fraction contains chlorite, smectite, mica, and kaolinite. Calcite, quartz, and siderite are also present in this unit.

Vitric silty claystone and vitric siltstone of Unit III contain traces of 1.4-nm clays in bulk samples, along with large amounts

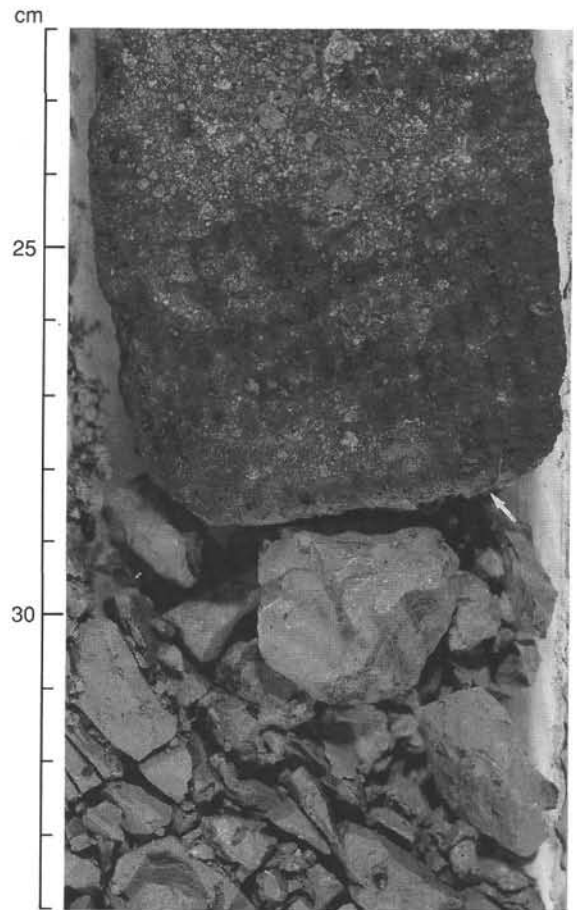


Figure 13. Vesicular base of lapilli tuff unit (indicated by arrow) shown in Figure 12. Interval shown is 126-787B-13R-3, 22–34 cm.

of feldspar, quartz, and calcite. Maghemite and halite (from pore water) are accessory minerals.

The silty claystone, clayey siltstone, and fine-grained sandstone in Subunit IVA are rich in smectite, with traces of mica (1.0 nm) and chlorite (Fig. 21A). Feldspar, calcite, quartz, and zeolite are also present. Clinoptilolite in clayey siltstone (Sample 126-787B-24R-1, 143 cm) is well crystallized (Fig. 21B). Clinoptilolite is a low-temperature alteration product commonly found in siliceous deep-sea sediments buried 100 m or more below the sediment/water interface (Kastner, 1979). A broad background in the XRD records indicates the presence of amorphous materials.

A nannofossil silty claystone in Subunit IVB contains a large amount of smectite with a trace of mica. Feldspar, quartz, and calcite are also present.

Sediment Accumulation Rates

Sedimentation rates for Site 787 were established from calcareous nannofossil ages and paleomagnetic data (Table 4), which were used to construct the age-depth curve shown in Figure 22. Sedimentation rates in the late Oligocene are 120 m/m.y. at the base of the hole (<30.3–27.74 Ma) and 26 m/m.y. in the interval between 27.01 and 24.21 Ma.

Most of the Miocene section was not recovered. Only a short interval of Zone CN8 appears to be present in Core 126-787B-5R. Similarly, only a short section of Pliocene sediment (3.5–4.6 Ma) was recovered; this interval has a sedimentation rate of 9.2 m/m.y. One nannofossil datum was present in the Pleisto-

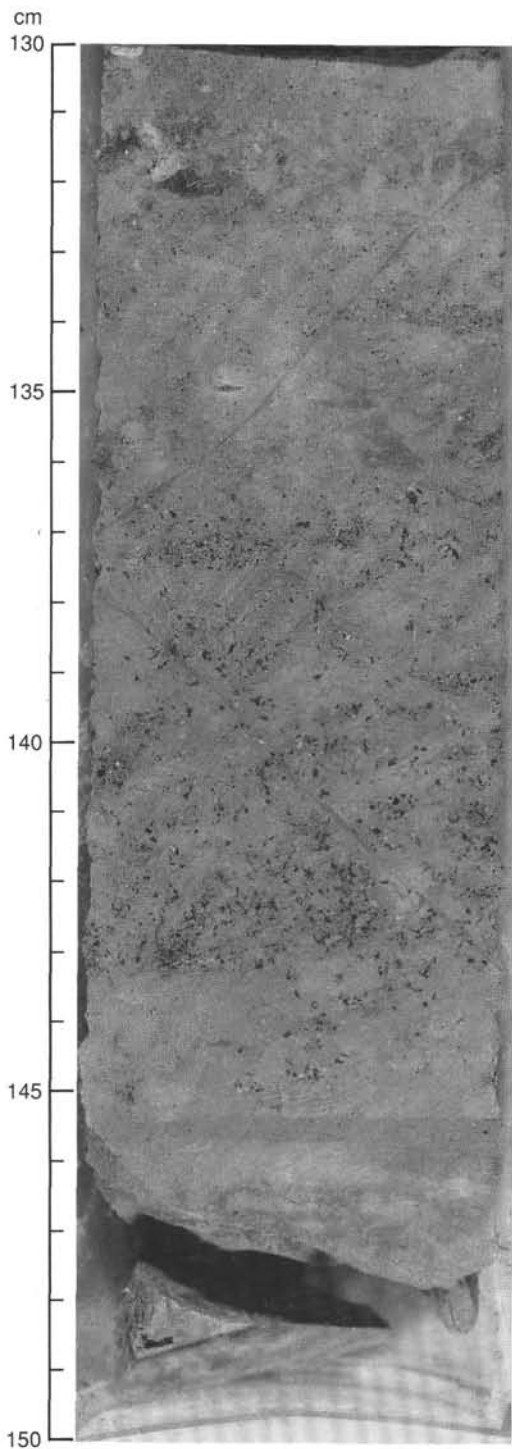


Figure 14. Black, sandy ash disseminated by bioturbation into nannofossil chalk. Interval shown is 126-787B-30R-1, 130-150 cm.

cene (first occurrence, or FO, of *Emiliana huxleyi*), giving an estimated sedimentation rate of 67.2 m/m.y. for the Quaternary. However, this rate may be suspect because we may not have recovered the surface (i.e., zero age) sediments.

Interpretation

Unit 1

The sandy gravels and sands that characterize this unit appear to form a veneer of coarse, volcanoclastic, unconsolidated

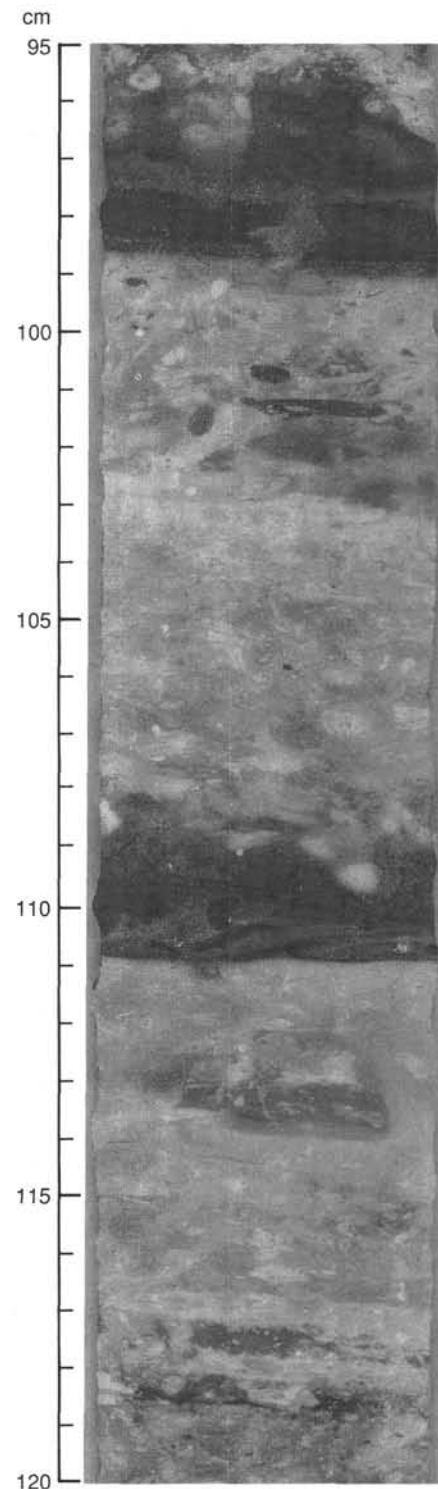


Figure 15. Black, lithic-crystal-vitric siltstone/fine sandstone beds (94-98.5 and 107-110.5 cm) with tops disrupted by bioturbation. The interval from 117 to 120 cm is probably a thin ash that has been almost completely disrupted by burrowers. Interval shown is 126-787B-25R-2, 95-120 cm.

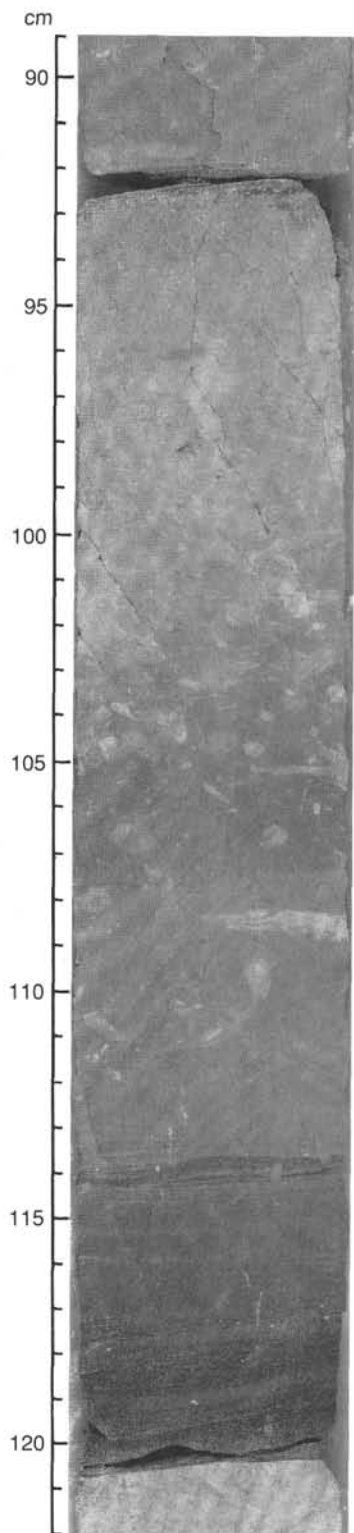


Figure 16. Graded silty sandstone to siltstone with wavy laminations, overlain by light-colored, bioturbated nannofossil-rich claystone, with burrows extending downward into the top of the clastic unit. Interval shown is 126-787B-29R-4, 89-122 cm.

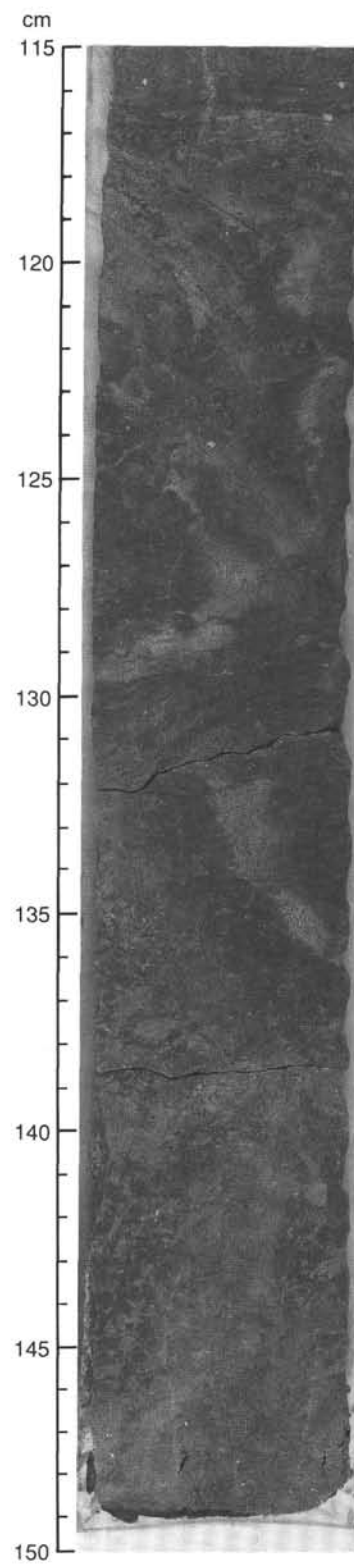


Figure 17. Plastically folded sandy mudstone and clayey siltstone in overturned section. Interval shown is 126-787B-21R-5, 115-150 cm.

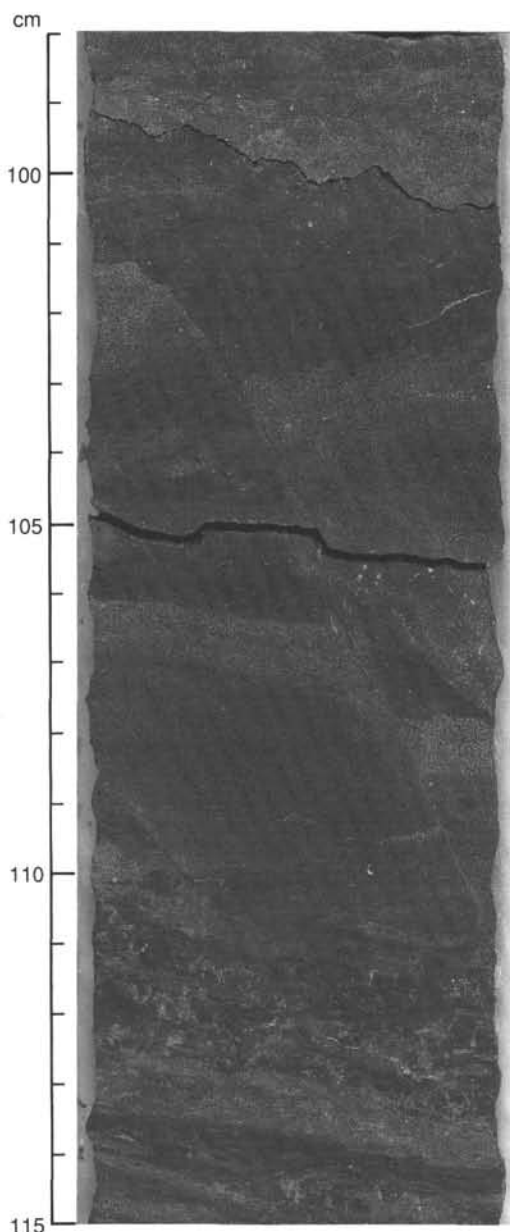


Figure 18. Extensional microfaults (apparent dips 45° – 60°) crosscutting very fine-grained sandstones and siltstones with apparent normal offset of 1–2 cm. Interval shown is 126-787B-21R-6, 98–115 cm.

material on the southern marginal terrace of Aoga Shima Canyon (see Figs. 3 and 4). Biostratigraphic data indicate an age of late Quaternary (<0.275 Ma) for Unit I, suggesting that sand and gravel are not being transported in Aoga Shima Canyon.

The texture of the material in Unit I and its location on the floor of a submarine canyon suggest transport by sediment gravity flows, perhaps high-concentration turbidity currents that were characterized by intense clast interactions (dispersive pressure) (Pickering et al., 1989).

Unit II

Recovery of this unit was very limited (4.5%). We interpret these nanofossil oozes and nanofossil-rich silty clays as pelagic or hemipelagic deposits. The vitric silt grains indicate fallout from volcanic eruptions along the volcanic arc.

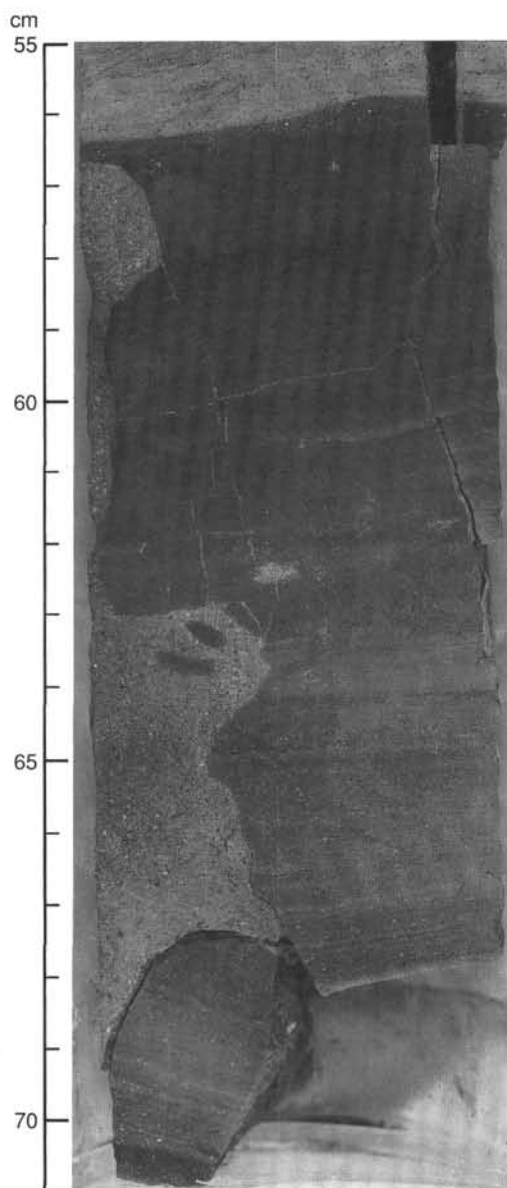


Figure 19. Sandstone injection into finely laminated silty claystone. The left-most, rotated, silty claystone piece at 67–70 cm was surrounded by sandstone (which occurs in the core catcher of Core 126-787B-21R) and was therefore detached from the wall of the sandstone dike. Interval shown is 126-787B-21R-7, 55–71 cm.

There is a marked difference in texture between Units I and II, and a sharp change in consolidation from Unit II to III, the latter being lithified. These contrasts, together with the biostratigraphic data (see “Biostratigraphy” section, this chapter), suggest that the upper and lower boundaries of Unit II are unconformities. The erosional surface between the rocks of Unit III and the soft sediments of Unit II may be part of the basal surface of a Miocene or Pliocene paleocanyon that cut into upper Oligocene rocks (Unit III).

Unit III

The fine-grained, strongly burrowed rocks of Unit III are predominantly hemipelagic sediments deposited in a distal, deep-water setting. The main sources of Unit III detritus were nanofossils that settled from the sea surface, infrequent fine-grained

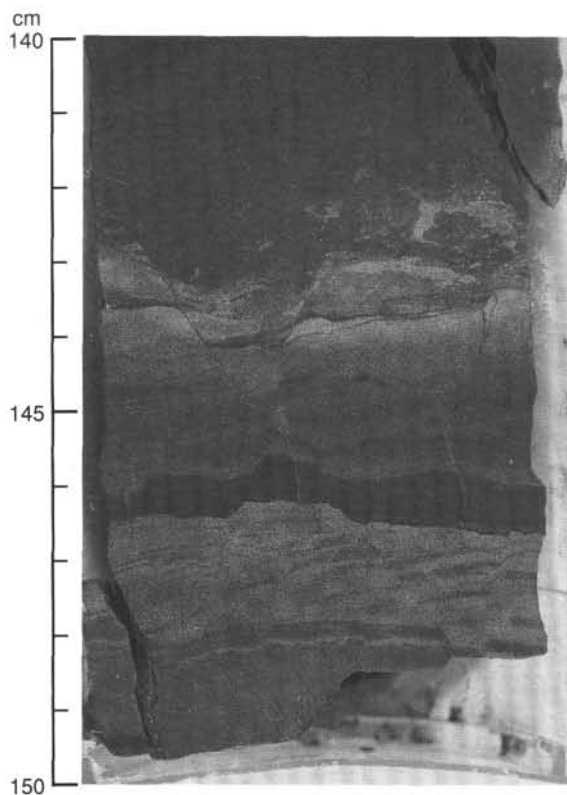


Figure 20. Conjugate fracture sets (apparent dips 45°–60°) in cross-laminated, very-fine-grained sandstone in the overturned interval of Core 126-787B-21R. Note the inverted graded bed at 143–146 cm. Interval shown is 126-787B-21R-6, 140–150 cm.

turbidity currents, and pulses of volcanic airfall from eruptions along the Izu-Bonin Arc or elsewhere in the western Pacific area. The lack of sandstone turbidites similar to those in Unit IV may indicate (1) relative quiescence of volcanic activity in the source area (i.e., along the Izu-Bonin Arc), (2) a shift in the direction of coarse-grained sediment supply after the deposition

of Unit IV, or (3) relative tectonic uplift of this area, with contemporaneous turbidity currents moving primarily along the deeper forearc-basin axis. The pyroclastic flow deposit near the base of Unit III and the presence of some disseminated ash within Unit III indicate some local (as well as regional) volcanicity at this time. The occurrence of turbidite sandstones of this age at Site 792, about 40 km to the west (see “Correlation and Comparison of Forearc Sites,” this volume), supports the second hypothesis.

The deformation fabrics in Unit III all formed in an extensional stress field. Movement on the microfaults is consistently extensional. The subvertical, kinked, veinlet structures are identical to those that Ogawa and Miyata (1985) interpreted to be extensional fracture cleavages formed in rapidly consolidating (wet) sediments. Clastic injections are also compatible with an extensional regime: early fractures were opened by extension and filled with poorly sorted, liquefied sediment.

Unit IV

We interpret the graded silty sandstone and siltstone beds in Subunit IVA, which show incomplete Bouma sequences (Bouma, 1962), as volcanoclastic turbidites. The interbedded massive and bioturbated finer grained sediments, including nannofossil-rich silty claystones and nannofossil-rich claystones, are primarily hemipelagic deposits. The bed thicknesses, sandstone/shale ratios, and sedimentary structures are typical of basin-plain turbidite settings (e.g., Ricci Lucchi and Valmori, 1980). Sedimentation rates were about 120 m/m.y. (Fig. 22), which is relatively low compared with rates for submarine fans and tectonically active basins of the California Borderland (Stow et al., 1985).

The slide unit in Core 126-787B-21R indicates a favorable combination of high water content in the sediment, probable seismic activity, and possibly bottom slopes of a few degrees in this part of the forearc basin. The paleoslope direction cannot be determined from the cores. After lithification, the sedimentary succession was fractured under extension, which accounts for the observed microfaults.

Subunit IVB contains significant thicknesses of structureless, volcanoclastic granule-rich and pebbly sandstone, interbedded with thin-bedded, fine-grained sandstones and siltstones that we interpreted as turbidites. Similar massive pebbly sand-

Table 3. X-ray diffraction data, Hole 787B.

Core, section interval (cm)	Unit	Color	Texture	Clay minerals (1.4–0.7 nm)	Minerals
126-787B-					
1R-CC, 4–6	I	10YR 6/6	Very coarse sand with yellowish clay	Bulk of clay parts chlorite + smectite < mica + kaolinite	Calcite > quartz > siderite Siderite is FeCO ₃
7R-1, 65	III	5Y 4/1	Dark gray vitric nannofossil-rich silty claystone	Bulk 1.4-nm traces	Feldspar > maghemite Quartz, calcite
10R-2, 94	III	5Y 7/2	Vitric siltstone (ash)	Bulk 1.4-nm clays	Calcite > quartz > halite
19R-5, 134	IVA	5GY 4/1	Silty claystone	Fine 1.482-nm abundant smectites Medium 1.499-nm common smectites Coarse 1.243-nm, trace	Feldspar, zeolite, amorphous materials
24R-1, 15	IVA	5G 2/1	Burrowed clayey siltstone with scattered sand grains	Bulk 1.482-nm abundant 1.0-nm traces 0.7-nm chlorite, traces	Feldspar, trace calcite Trace quartz
24R-1, 143		5G 2/1	Burrowed clayey siltstone with pods of fine sand (ash?)	Bulk 1.4-nm traces 1.0-nm traces 0.7-nm chlorite, traces	Calcite, clinoptilolite, feldspar
25R-4, 112–113	IVA	5Y 2.5/1	Very dark gray very fine sandstone to siltstone	Bulk 1.43-nm abundant 0.7-nm chlorite, trace	Calcite, mordenite, or stilbite, Feldspar
33R-2, 104–107	IVB	N5	Nannofossil silty claystone	Bulk 1.497-nm abundant 0.999-nm mica, trace	Feldspar > quartz > calcite 0.8458-nm, trace

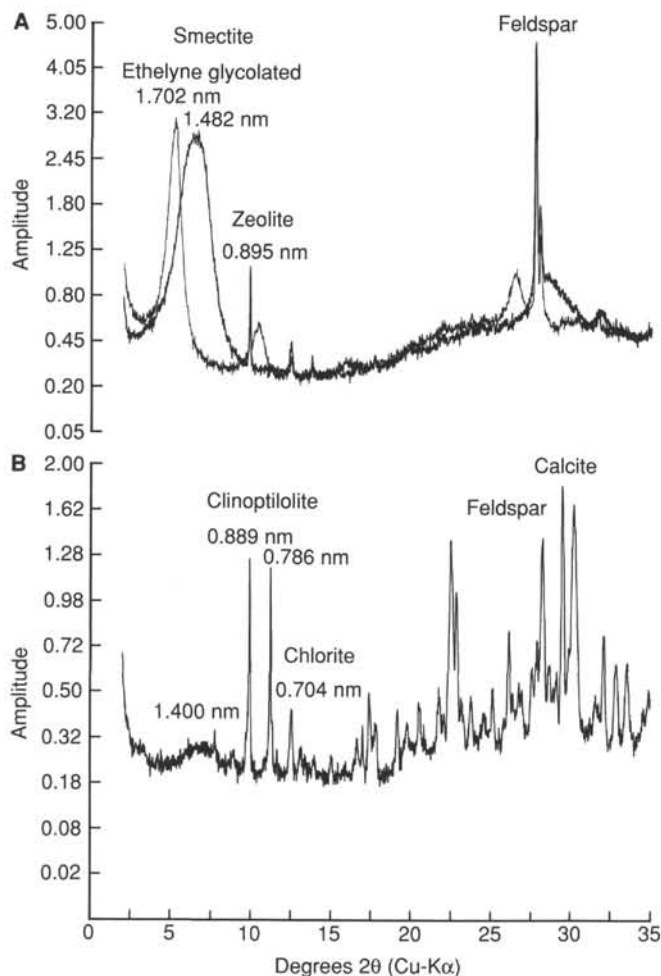


Figure 21. X-ray diffraction analyses. **A.** Sample 126-787B-19R-5, 134 cm, showing a large amount of smectite with feldspar and zeolite. The 1.482 nm peak was shifted to 1.702 nm by ethylene glycol treatment. **B.** Sample 126-787B-24R-1, 143 cm, showing large amounts of clinoptilolite, feldspar, and calcite with a small amount of chlorite (0.704 nm) and a trace of 1.4-nm minerals.

stones, which include large intraclasts of silty claystone, are typically present in channelized units in well-documented ancient successions (Nilsen and Abbott, 1981).

BIOSTRATIGRAPHY

Calcareous Nannofossils

Hole 787A

Sample 126-787A-1W-CC contains *Discoaster berggrenii*, *D. bollii*, *D. loeblichii*, and *D. calcaris*. Ordinarily, the ranges of these species do not overlap but occur in adjacent zones (Zones CN7, CN8, and CN9) in the upper Miocene. However, this sample was from a core catcher at the bottom of a washed hole, and the species could easily have been mixed together as a result of drilling.

Hole 787B

Samples 126-787B-1R-CC through 126-787B-3R-CC contain *Gephyrocapsa oceanica* and *Emiliana huxleyi*, and fall within Zone CN15 (late Quaternary). This interval contains a moderate amount of reworked Pliocene and Miocene species, such as *Re-*

Table 4. Chronostratigraphic data, Hole 787B.

Biostratigraphic event ¹	Core, section, interval (cm) (126-787B-)	Depth (mbsf)	Age (Ma)
Calcareous nannofossils			
<i>Emiliana huxleyi</i>	FO 3R-CC	15.51–21.47	<0.275
<i>R. pseudumbilica</i>	LO 4R-1, 7–8	15.51–21.47	3.5
<i>C. rogosus</i>	FO 5R, 10–11	31.00–40.30	4.6
<i>R. bisecta</i>	LO 6R, 82–88	31.29–41.10	ca. 23.7
<i>S. distensus</i>	LO 27R-CC	250.7–252.7	28.2
<i>S. ciproensis</i>	FO 34R-CC	320.1	<30.3
Paleomagnetic events			
Base of third normal in Anomaly 6c	7R, 130	51.1–58.8	24.21
Top of second normal in Anomaly 8	14R/15R-2	121.7–131.5	27.01
Base of second normal in Anomaly 8	19R-4, 50	170.8–171.04	27.74
Top of first normal in Anomaly 9	25R-4, 110	229.3–230.78	28.15
Base of first normal in Anomaly 9	31R/32R	283.5–298.2	28.74
Biostratigraphic zones			
Nannofossil Zone CN8	5R-CC	30.9–40.3	8.2–8.9

¹ FO = first occurrence, LO = last occurrence.

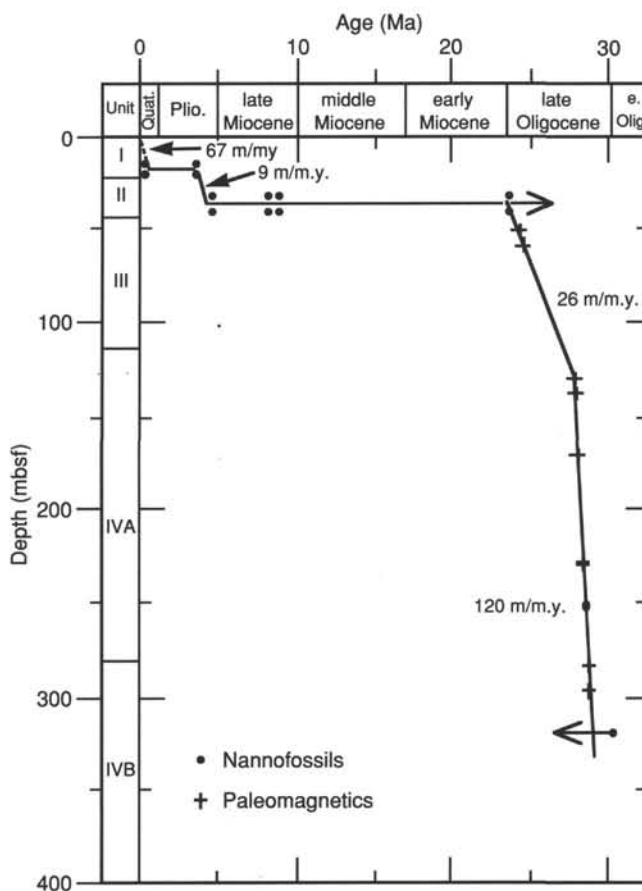


Figure 22. Age-depth plot of paleomagnetic and nannofossil data for Hole 787B. Upper and lower depth limits are given for each biostratigraphic and paleomagnetic datum. See Table 4 for details.

reticulofenestra pseudoumbilica, *Discoaster brouweri*, *D. variabilis*, *D. pentaradiatus*, *D. berggrenii*, and *Calcidiscus macintyreii*.

Samples 126-787B-4R-1, 7–8 cm, -4R-2, 4–5 cm, -4R-CC, and -5R-1, 10–11 cm, contain *Reticulofenestra pseudoumbilica*, *Sphenolithus abies*, *Discoaster variabilis*, *D. surculus*, *D. brouweri*, *Pseudoemiliania lacunosa*, and *Ceratolithus rugosus*, which would place them in the lower Pliocene Zones CN10C–CN11. These samples also contain moderate amounts of reworked Miocene species, such as *Discoaster berggrenii*, *D. quinqueramus*, *D. loeblichii*, *D. deflandrei*, and *Minylitha convallis*.

Sample 126-787B-5R-CC contains *Minylitha convallis*, *Discoaster neohamatus*, and *D. bergeni*, and is constrained to upper Miocene Zone CN8. Other species present are *Discoaster brouweri*, *D. prepentaradiatus*, *D. icarus*, *D. pentaradiatus*, *D. variabilis*, *Reticulofenestra pseudoumbilica*, *Coccolithus pelagicus*, *Calcidiscus leptoporus*, and *Sphenolithus moriformis*.

Samples 126-787B-6R-1, 87–88 cm, through -34R-CC are located between the last occurrence (LO) of *Reticulofenestra bisecta*, marking the Oligocene/Miocene boundary, and the first occurrence (FO) of *Sphenolithus ciperoensis*, which marks the base of upper Oligocene Zone CP19. The LO of *Sphenolithus distentus*, which marks the boundary between Subzones CP19A and CP19B, occurs in Sample 126-787B-27R-CC. The Oligocene sediments in Hole 787B contain a low-diversity assemblage with moderate preservation throughout most of the section, with scattered samples exhibiting higher diversity. Typical species in this interval include *Discoaster deflandrei*, *D. calculosus*, *D. adamanteus*, *Coccolithus pelagicus*, *Reticulofenestra bisecta*, *Cyclicargolithus floridanus*/*C. abisectus*, and *Sphenolithus moriformis*.

The abundance of discoasters in the upper Miocene and upper Oligocene sections of Holes 787A and 787B suggest warm-water conditions during the corresponding time intervals.

Planktonic Foraminifers

Hole 787B

Cores 126-787B-1R, -2R, and -3R are assigned to Zone N22 of early Pleistocene age, given the presence of rare *Globorotalia truncatulinoides* and *G. menardii* (sinistral), and the absence of *Globigerinoides ruber* (pink), *G. calida calida*, and *Pulleniatina finalis*.

Sample 126-787B-4R-CC contains rare specimens of *Globorotalia tosaensis* and *Sphaeroidinella dehiscens*, placing it in Pliocene Zones N19–N21.

The Pleistocene and Pliocene assemblages are dominated by *Globorotalia inflata* and *Globigerinoides* spp.

Sample 126-787B-5R-CC contains rare specimens of *Globorotalia plesiotumida*, *G. merotumida*, *Globigerina* cf. *falconensis*, and *G. druryi*, placing this sample in the upper Miocene Zones N16–N18.

A single specimen of *Catapsydrax dissimilis* (upper Oligocene to lower Miocene range) was present in Sample 126-787B-19R-CC.

The planktonic foraminiferal assemblages do not show dissolution effects under the reflected-light microscope at about 100X magnification. The fair to good preservation of foraminifer shells is probably the result of rapid clastic sedimentation rates.

Paleoceanography

The planktonic foraminifer assemblages in Quaternary Samples 126-787B-1R-CC and -2R-CC are represented by warm-water taxa such as *Globigerinoides sacculifer*, *G. ruber*, *G. quadrilobatus*, *G. conglobatus*, *Pulleniatina obliquiloculata*, and *Globorotalia menardii*, as well as by cooler water species including *Globigerina bulloides*, *G. pachyderma* (dextral), *Globigerinita*

glutinata, and *Globigerina quinqueloba*. These two intervals are preceded in Sample 126-787B-3R-CC by colder water faunas dominated by *Globorotalia truncatulinoides* and *Globorotalia inflata*, with less abundant *G. bulloides* and dextral *G. pachyderma*. Warm-water taxa occur in lower abundances in this sample.

The paleotemperatures indicated by the upper Pliocene faunas (Core 126-787B-4R) were probably somewhat higher than those that prevailed during the deposition of sediments in Core 126-787B-3R. We make this interpretation given the dominance of the *Globorotalia menardii* group, globigerinoids, and *Sphaeroidinopsis* spp., as well as the lower abundances of globigerinids. As several representative species in this core are extinct, our interpretation is tentative, pending confirmation by $\delta^{18}\text{O}$ measurements. Sample 126-787B-5R-CC contains cold and warm surface and subsurface morphotypes. Water paleotemperatures were slightly higher for this sample than for the late Pliocene. Our basis for this assumption, to be confirmed by oxygen-isotope measurements, is the predominance of menardiform globorotalids, globigerinoids, and *Sphaeroidinopsis* spp., as well as the lower abundances of globigerinids.

Benthic Foraminifers

Samples 126-787B-1R-CC through -5R-CC contain *Cibicides wellerstorfi* and are correlative with the cosmopolitan benthic foraminiferal Zone CD4 (Kaiho, in press), which corresponds to the post-middle middle Miocene turnover event. This fauna is characterized by deep-oceanic taxa such as *C. wellerstorfi*, *Oridorsalis umbonatus*, *Melonis barleeanus*, *Hoeglundina elegans*, *Pleurostomella* spp., *Pullenia bulloides*, *Uvigerina* spp., *Pyrgo* sp., and *Epistominella exigua*. The presence of these taxa indicates depositional water depths of 2000–4000 m and normal oxygen conditions in the surface sediments. Sample 126-787B-3R-CC contains the inner neritic species *Elphidium crispum*, which was probably transported from shallower depths.

Benthic foraminifers from Samples 126-787B-8R-1, 32–34 cm through -27R-CC are rare, moderately preserved, and include *Cibicides* sp., *Oridorsalis umbonatus*, *Pullenia bulloides*, *Stilostomella* spp., *Pleurostomella* spp., and *Chrysalogonium* sp. The presence of these calcareous species and rare planktonic foraminifers indicates depositional water depths of 3000–4000 m. The absence of *C. wellerstorfi* and *Nuttallides truempyi* in these samples allows assignment to Zone CD3, which corresponds to the interval between the LO of *N. truempyi* (near the middle/upper Eocene contact) and the FO of *C. wellerstorfi* (middle middle Miocene).

Radiolarians

Quaternary sediments from Site 787 contain abundant radiolarians. With the exception of rare, poorly preserved specimens in Core 126-787B-13R, identifiable radiolarians are absent below Core 126-787B-5R, although we commonly observed infilled and highly corroded radiolarian ghosts.

An abundant and well-preserved radiolarian assemblage was recovered from Samples 126-787B-1R-CC through -3R-CC. This assemblage contains *Lamprocyclus maritimus*, *Anthocyrthidium angulare*, *Axoprunum angelinum*, *Theocorythium trachelium*, and *Eucyrtidium calvertense* and is typical of the lower Pleistocene *Anthocyrthidium angulare* Zone.

Sample 126-787B-5R-CC contains a radiolarian assemblage that is diluted by volcanogenic debris. This assemblage includes *Diartus hughesi*, which indicates the upper Miocene *Didymocyrtis antepenultima* Zone.

A single identifiable specimen *Lithocyclia angusta* was recovered from Sample 126-787B-13R-CC. The specimen is poorly preserved but permits tentative assignment to the upper Oligocene *Dorcadospyris atechus* Zone.

Summary

Biostratigraphy

A summary of the biostratigraphic results for Site 787 is presented in Figure 23.

We washed Hole 787A down to 34.5 mbsf and recovered one core-catcher sample, which contained the upper Miocene calcareous nannofossils *Discoaster bollii*, *D. loeblichii*, *D. calcaris*, and *D. berggrenii*.

The presence of the calcareous nannofossil *Emiliana huxleyi* in Cores 126-787B-1R, -2R, and -3R indicates a late Quaternary age for this interval. Some reworking is evidenced by the presence of early Pliocene or older calcareous nannofossils, planktonic foraminifers, and radiolarians. This interval corresponds to Unit I (see "Lithostratigraphy and Accumulation Rates," this chapter).

The interval from Samples 126-787B-4R-1, 7-8 cm, to -5R-1, 10-11 cm, contains a calcareous nannofossil assemblage indicative of the lower Pliocene (Zones CN10C-CN11). The planktonic foraminifers in Sample 126-787B-4R-CC are indicative of the lower to upper Pliocene (Zones N19-N21). Therefore, this interval is assigned an early Pliocene age.

Sample 126-787B-5R-CC is assigned a late Miocene age on the basis of calcareous nannofossils, planktonic foraminifers, and radiolarians. A hiatus probably separates this sample from the overlying Pliocene sediments, but because of poor core recovery in Core 126-787B-5R we cannot estimate the extent of this hiatus. The Miocene and Pliocene sediments correspond to

Unit II (see "Lithostratigraphy and Accumulation Rates," this chapter).

Interval 126-787B-6R-1, 87-88 cm, through -34R-CC is assigned a late Oligocene age, primarily on the basis of calcareous nannofossils. The low-diversity assemblage contains *Reticulofenestra bisecta*, *Discoaster deflandrei*, *D. calcosus*, *Cyclicargolithus floridanus/C. abisectus*, *Sphenolithus ciproensis*, and *S. distentus*. Single specimens of the planktonic foraminifer *Catapsydrax dissimilis* in Sample 126-787B-19R-CC and the radiolarian *Lithocyclus angusta* in Sample 126-787B-13R-CC also corroborate the late Oligocene age assignment for this interval. This interval corresponds to Unit III and Subunits IVA and IVB (see "Lithostratigraphy and Accumulation Rates," this chapter) and is separated from the overlying Miocene sediments by a hiatus of at least 14.8 m.y.

Paleoenvironments

Planktonic foraminiferal evidence suggests that surface-water temperatures were warm in the Pliocene and Quaternary, except for a cooler interval in Core 126-787B-3R (Quaternary), when the colder water species *Globorotalia truncatulinoides* and *G. inflata* dominated the fauna. The dominance of the *Globorotalia menardii* group, globigerinoids, and *Sphaeroidinellopsis* spp. suggest warm-water conditions in the late Miocene. An abundance of discoasters in the Miocene and Oligocene intervals also indicates warm-water conditions during these times.

The calcareous benthic foraminiferal fauna indicates deep-oceanic conditions (lower bathyal to upper abyssal depths; >2000

Depth (mbsf)	Core	Calcareous nannofossils	Planktonic foraminifers	Radiolarians	Benthic foraminifers (zones and paleobathymetry)		Age
0	2R	CN15	N22	<i>A.angulare</i>	CD4	2,000 – 4,000 m	Quaternary
	3R						
	4R						
	5R	CN10C-CN11	N19-N21	?			early Pliocene
	6R	CN8	N16-N18	<i>D. antepenultima</i>			late Miocene
	7R	CP19B					late Oligocene
	8R						
	9R						
	10R						
	11R						
100	12R						
	13R						
	14R						
	15R						
	16R						
	17R			<i>D. ateuchus</i>			
	18R						
	19R		u. Oligocene – l. Miocene				
	20R						
	21R						
200	22R						
	23R						
	24R						
	25R						
	26R						
	27R						
	28E						
	29R						
	30R						
	31R	CP19A					
	32R						
300	33R						
	34R						
							Barren

Figure 23. Summary of the biostratigraphic and paleobathymetric results for Hole 787B.

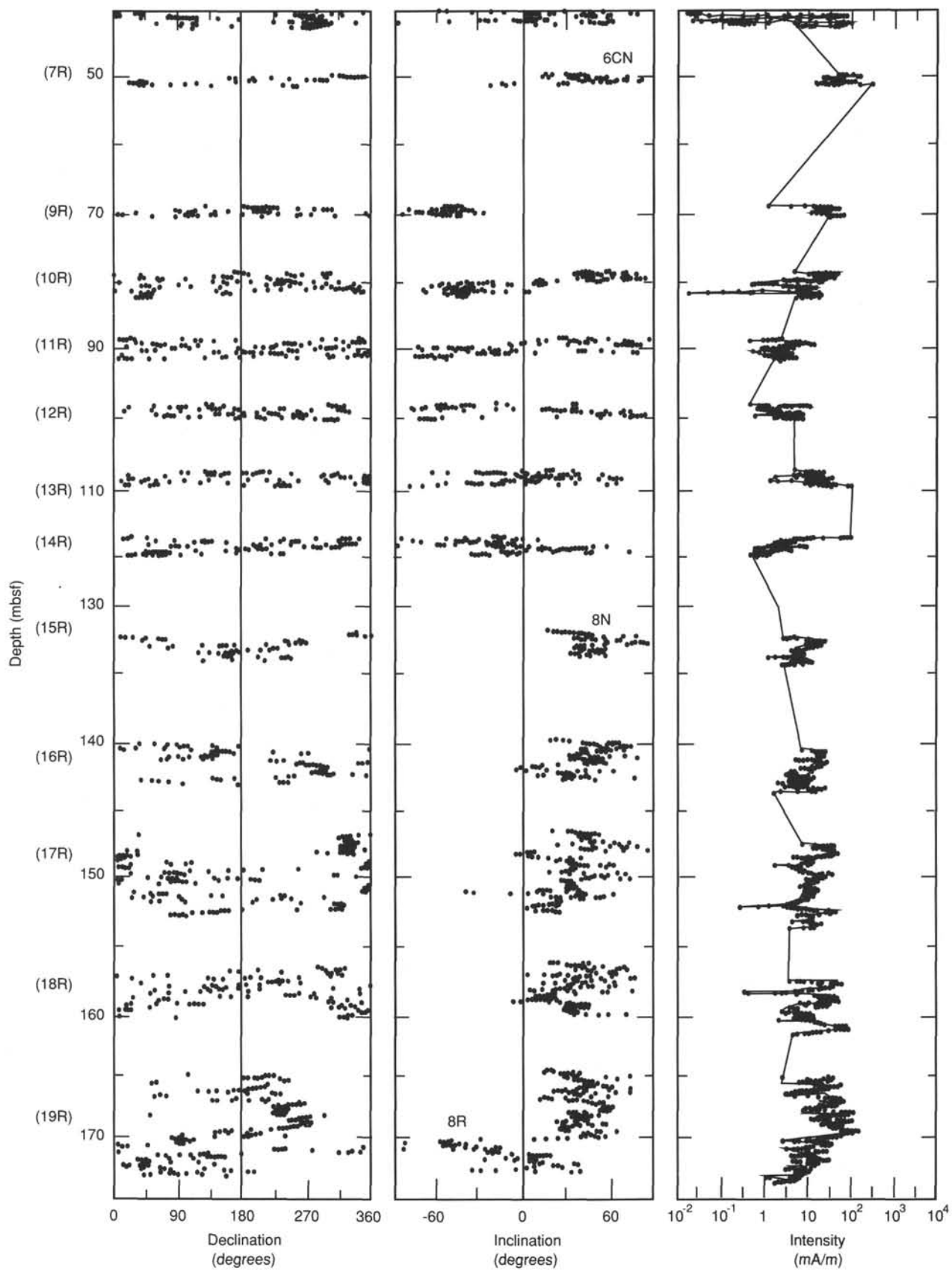


Figure 24. Paleomagnetic results vs. depth (mbsf) for Hole 787B. All data are obtained after optimum AF demagnetization. Core numbers are indicated in parentheses. Probable beginnings of polarity chrons are indicated with inclination data.

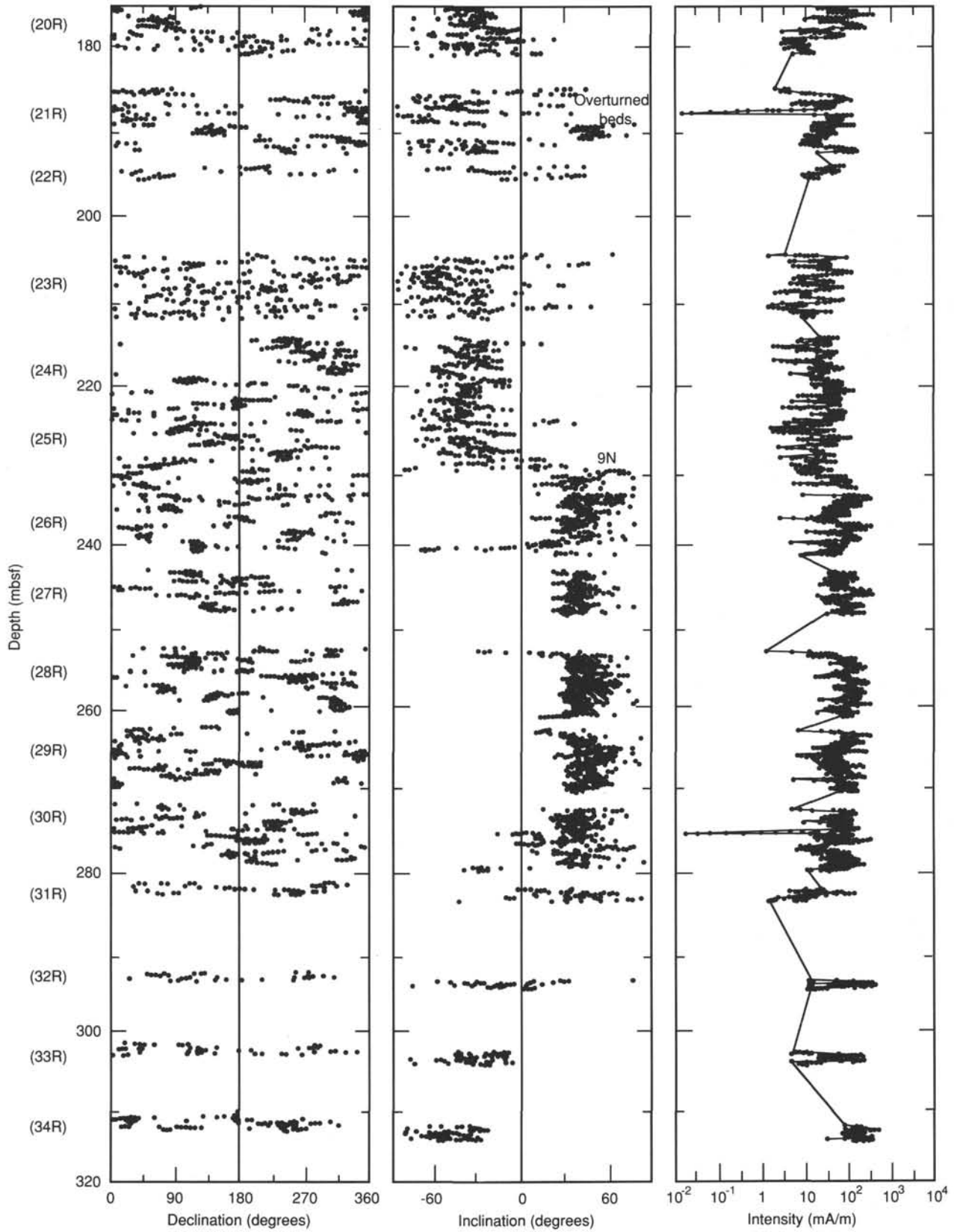


Figure 24 (continued).

m and above the CCD) during most of the depositional interval at Site 787. In Samples 126-787B-3R-CC and -5R-CC, the inner neritic species *Elphidium crispum* indicates downslope transport from shallow waters.

PALEOMAGNETISM

Introduction

To establish the magnetostratigraphy and detect possible latitudinal movement of Site 787, we measured the remanent magnetization of the cores. We measured most archive halves with the 2G-Enterprises pass-through cryogenic magnetometer. Several discrete samples were also measured using the Molspin magnetometer and the Fully Automatic Spinner (FAS) magnetometer (see "Explanatory Notes" chapter, this volume). Archive halves were subjected to alternating field (AF) demagnetization using the three-axial-coil system attached to the cryogenic magnetometer. Discrete samples were stepwise demagnetized using a Schonstedt AF Demagnetizer or the AF demagnetizer attached to the FAS magnetometer.

Magnetostratigraphy

Hole 787B

The natural remanent magnetization (NRM) of most archive halves from Hole 787B was measured at 3-cm intervals. Magnetic directions and intensity after the highest AF demagnetization step are shown in Figure 24. Declinations are arbitrary because all cores were drilled with an unoriented rotary core barrel.

A primary component of remanent magnetization generally appears to be preserved in the cores. The NRM intensities decreased by 10%–50% after 15-mT AF demagnetization for almost all claystone and siltstone samples. The weaker, coarse-grained sandstone samples are much less resistant to AF demagnetization; therefore, to preserve some magnetic signal in the archive halves, we used lower maximum alternating fields (2–8 mT). The NRMs of the sandstones were commonly overprinted with a present-field normal component of magnetization that masked the polarity of the primary remanence; the claystones were less commonly overprinted. In general, AF demagnetization was effective in removing this "soft" component to reveal the underlying primary polarity (Fig. 25).

The first three cores from this hole were coarse grained and highly disturbed, so we did not measure their remanence. After AF demagnetization, we could discern several short and long magnetic-polarity intervals for some of the core segments measured (Fig. 24). We divided the magnetostratigraphy of the site into four parts, accordingly: (1) the upper part (Sections 126-787B-4R-1 to -14R-3) was characterized by incomplete recovery and has several short normal/reversed intervals; (2) the upper-middle part (Sections 126-787B-15R-1 to -19R-4) is a long, normal-polarity interval; (3) the lower-middle part (Section 126-787B-19R-4 to -25R-4) is dominated by reversed polarity (note that the onset of a short, normal-polarity interval at Sample 126-787B-21R-5, 115 cm [189.5 mbsf; Fig. 24], correlates with an overturned slump unit [see "Lithostratigraphy and Accumulation Rates," this chapter, Fig. 17]); and (4) the lower part (Sections 126-787B-25R-4 to -34R-2) is characterized by a long, normal-polarity interval with a zone of reversed polarity at the bottom of the hole.

We carried out additional NRM measurements and stepwise AF demagnetizations on selected discrete samples collected from the working halves to examine the stability of remanent magnetization (Table 5). Many of these samples have a dominant, pri-

mary component of NRM that one can discern after removal of a "soft" secondary component (Fig. 26). These results confirm the validity of the polarity sequence obtained from our measurement of the archive halves. The magnetization associated with the bioturbated claystones appears to be consistent in both direction and intensity with that of the finely laminated intervals, indicating that the remanent magnetization was acquired after deposition and bioturbation.

According to the biostratigraphic ages of the cores (see "Biostratigraphy," this chapter), the age of the upper part of Hole 787B ranges from late Oligocene to Pliocene, whereas the age of the other three parts is late Oligocene (nannofossil Zone NP24 or NP25). The normal-polarity interval associated with the top of Unit III (Core 126-787B-7R, ~50 mbsf) may represent the bottom part of normal-polarity Chron 6C (Fig. 27). If this is true, then the many short normal- and reversed-polarity intervals recorded in the underlying cores would be the result of hiatuses in sedimentation and/or the rapid magnetic reversal rate in the mid-late Oligocene. Because paleontological datums are absent within the upper upper Oligocene (see "Biostratigraphy," this chapter), a firm polarity chron assignment within this zone is not possible. For the lower three parts of the hole, we correlate the long N-R-N-R polarity interval sequence with Chrons 8N, 8R, 9N, and the short reversed zone within 9N (Fig. 27), on the basis of the nannofossil biochronology (see "Biostratigraphy," this chapter).

In general, magnetization is assumed to have been acquired sequentially in an upward direction. The correlation between the sharp polarity reversal and the beginning of the slump unit in Section 126-787B-21R-3 (centered at 190 mbsf; Fig. 24) indicates that magnetization was acquired before the slumping event. However, in Section 126-787B-26R-5 (~240 mbsf), a short interval of reversed polarity (55–110 cm) occurs in the upper half of the long-normal-polarity Chron 9N. This reversed interval correlates precisely with an unusual zone of diffuse bedding laminations (Fig. 28), suggesting a restricted zone of remagnetization associated with diagenesis, and having remanence acquired after the polarity of the magnetic field had reversed.

Paleolatitude

The mean inclination values shown in Figure 24 are approximately 40°, although in Core 126-787B-28R, zones of low scatter have inclinations of ~32° (Fig. 29). These data indicate that Site 787 was situated at a latitude of 17°N in middle Oligocene time, which is 15° lower than the present latitude for this site. This implies that the Site 787 locale has been shifted from an area of lower latitude by plate motion, as may be the case for the West Philippine Basin (Louden, 1977) and the Daito Ridge (Kinoshita, 1980).

SEDIMENT/FLUID GEOCHEMISTRY

Nine 10-cm-long, whole-round samples were obtained from Hole 787B for electrical resistivity measurements, pore-water squeezing, and sediment and fluid analyses.

The headspace hydrocarbon analyses did not show any gases above background level and thus are not reported.

Sediment Resistivity

The formation factors calculated from the resistivity measurements vary between 4.8 and 28.6 (Table 6), and the vertical distribution exhibits a pronounced maximum at 130.3 mbsf (Section 126-787B-15R-2; Fig. 30). This section consists of a strongly lithified silty sandstone. In general, formation factors in claystones and mudstones vary between 8 and 20. It is possible that the maximum reading has been affected by the measurement

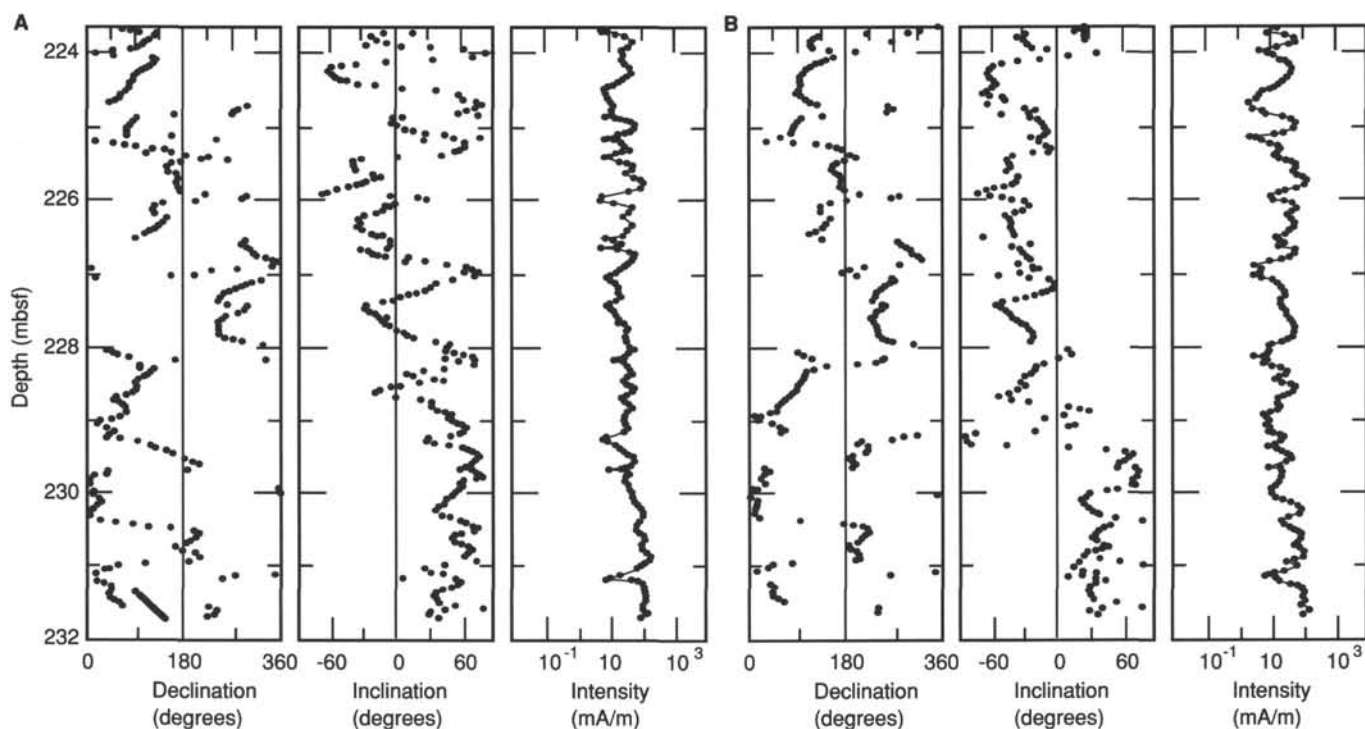


Figure 25. Paleomagnetic results for Core 126-787B-25R. **A.** Before AF demagnetization to 15 mT. **B.** After demagnetization.

Table 5. Remanence properties of discrete samples, Hole 787B.

Core, section, interval (cm)	Optimum AF (mT)	Inc. (deg)	J_0 ($\times 10^{-3}$ mA/M)	J_{AF}	Lithology
126-787B-					
4R-1, 22	100	+45	59.4	8.67	Clay
5R-1, 22	30	+43	128.0	7.72	Clay
7R-1, 11	45	+38	128.0	41.4	Claystone
7R-2, 3	25	+49	42.0	26.6	Clay
13R-1, 36	50	-35	72.6	12.4	Agglomerate
13R-1, 104	50	-32	57.5	14.4	Agglomerate
13R-3, 87	30	+42	119.0	23.5	Claystone
14R-2, 37	30	+48	3.75	0.44	Sandstone
14R-3, 43	10	+50	7.86	3.70	Sandstone
15R-2, 22	15	+44	5.98	1.45	Sandstone
15R-4, 39	30	+44	27.0	13.3	Claystone
16R-4, 61	15	+42	11.6	12.4	Siltstone

procedure, which involves drilling holes for the electrodes. Although the exact magnitude of the maximum may be dubious, its presence is supported by neighboring data.

Sediment Geochemistry

Sediments from Site 787 were analyzed on board ship for inorganic carbon and total carbon and nitrogen (see "Explanatory Notes," this volume), and these data are presented in Table 7. The carbonate analyses are reported in the physical property section. The concentration of organic carbon in Hole 787B is generally <0.5%. There is an overall decrease of organic carbon from the top to the bottom of the hole. The concentration of total nitrogen varies between 0.06% and less than the detection limit.

Fluid Geochemistry

Because we drilled Hole 787B with the RCB, we paid special attention to possible contamination of the pore water by drill-

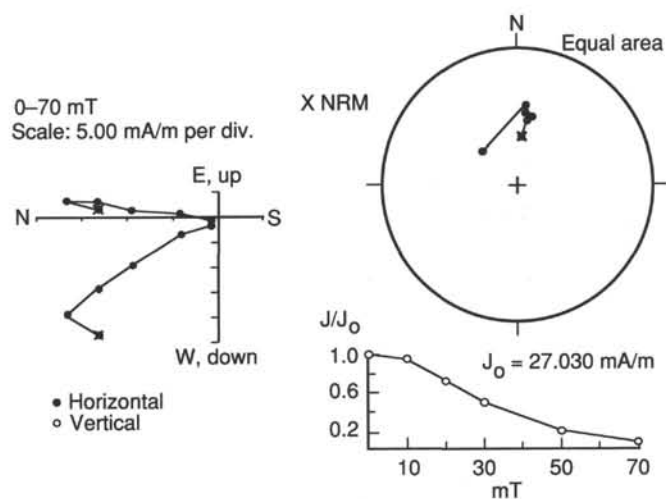


Figure 26. Example of change of NRM direction, intensity, and orthogonal components of magnetization with AF demagnetization, Sample 126-787B-15R-4, 39 cm.

ing-mud filtrate. Starting with Core 126-787B-4R, drilling mud was used during the drilling of alternate cores. The analytical results presented in Table 8 show that the drilling-mud filtrate has a chloride concentration about 1/20 of the pore waters. Thus, the comparatively low concentrations of sodium and chloride in the sample from Section 126-787B-12R-1 probably reflect some mixing with drilling-mud filtrate.

Qualitatively, the distribution of dissolved constituents in the upper 140 m of the sediment is typical of most deep-sea sediments and includes decreasing potassium and magnesium concentrations (Fig. 31) and increasing concentrations of calcium and strontium. These changes are related to reactions involving

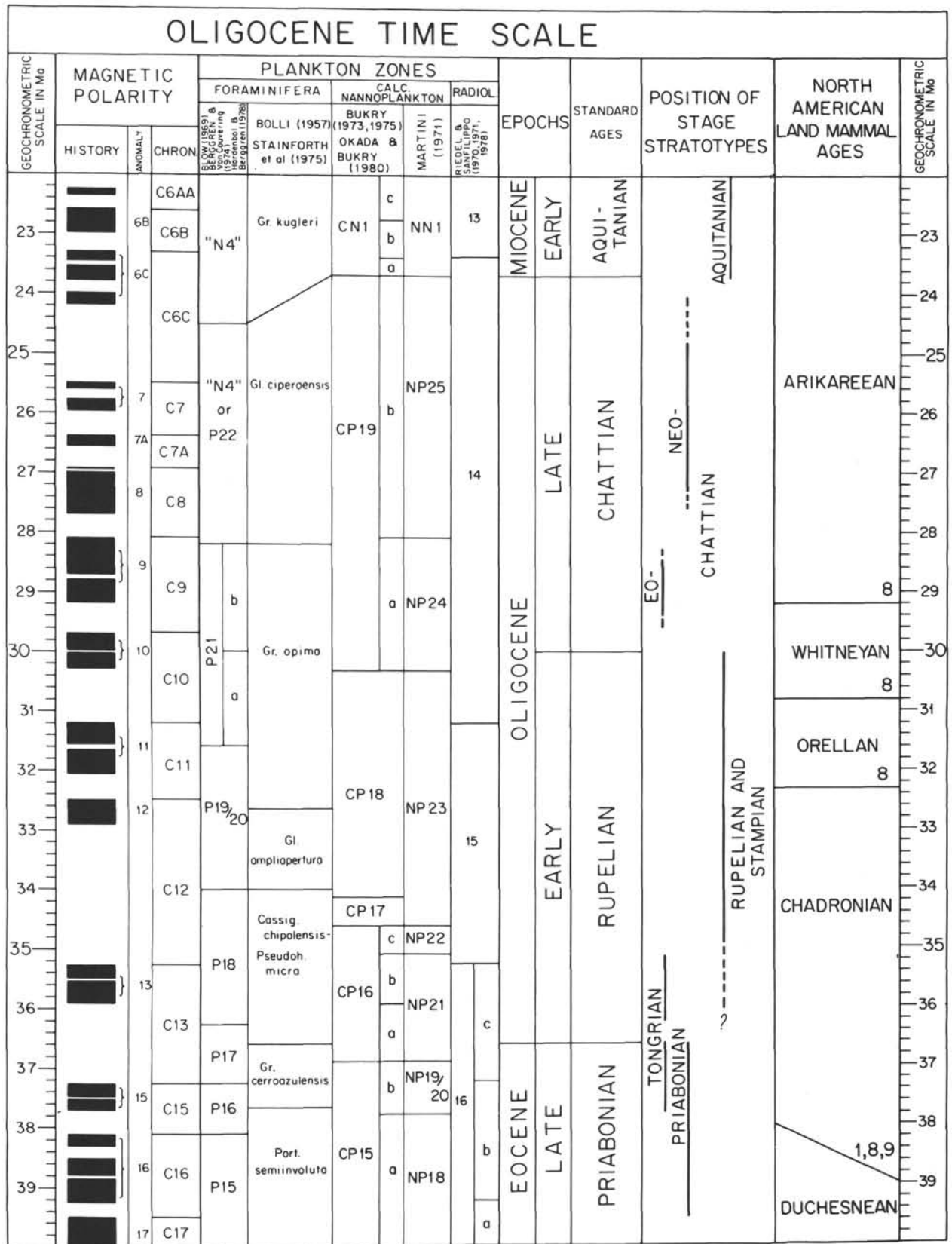


Figure 27. Oligocene time scale (from Berggren et al., 1985).

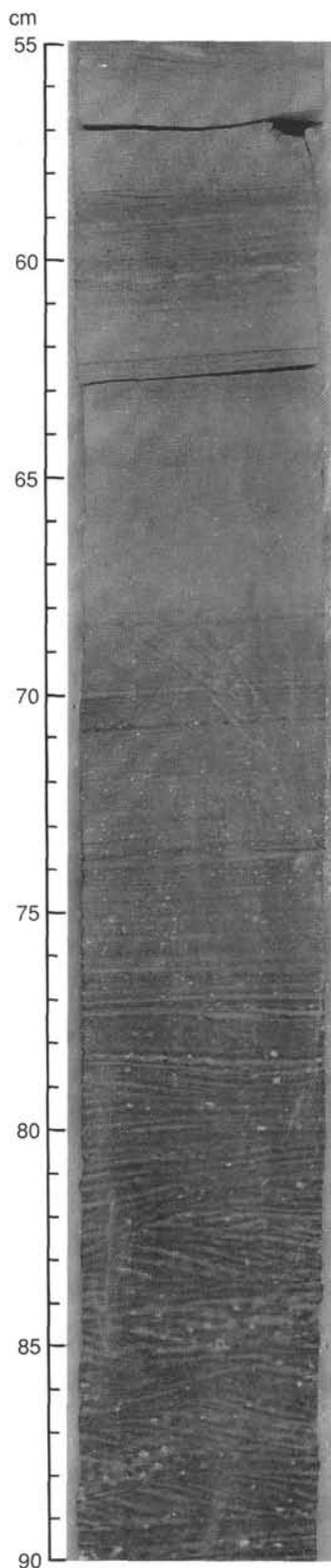


Figure 28. Transition from normal to diffuse bedding laminations, Interval 126-787B-26R-5, 55-90 cm. The laminations correlate to a zone of anomalous magnetic polarity in Section 126-787B-26R-5.

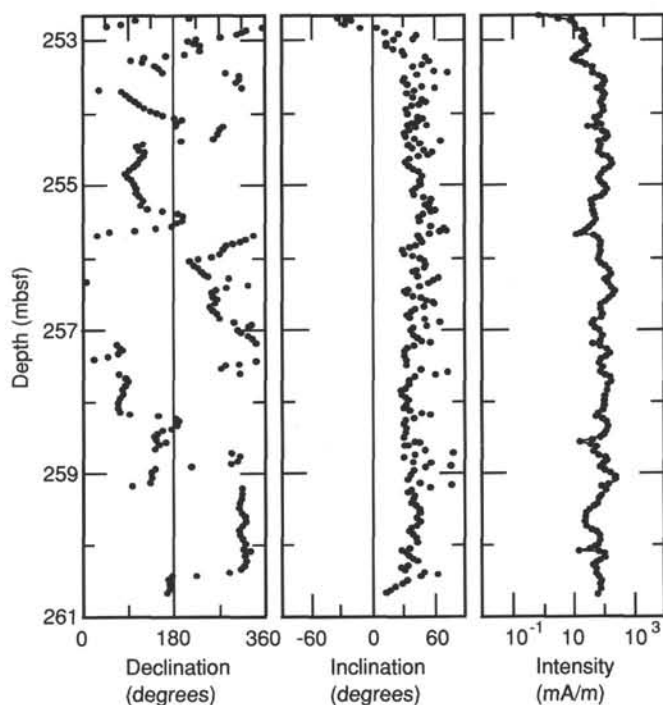


Figure 29. Paleomagnetic results, after AF demagnetization to 15 mT, for Core 126-787B-28R.

Table 6. Sediment resistivity, measurement temperature, pore-water resistivity at 25°C, and formation factor of sediments from Hole 787B.

Core, section, interval (cm)	Depth (mbsf)	K_c (m)	R_s (ohm-m)	t (°C)	R_{pw} (ohm-m)	F
123-787B-						
9R-2, 65-75	71.20	0.1007	1.33	13.5	0.198	4.8
12R-1, 3-13	98.18	0.0946	1.49	14.9	0.204	5.0
15R-2, 146-156	130.21	0.0908	8.23	14.9	0.198	28.6
18R-1, 80-90	157.05	0.1031	4.59	11.9	0.192	17.7
21R-2, 140-150	187.95	0.1050	2.65	11.4	0.195	10.2
24R-2, 140-150	217.05	0.0959	2.81	13.1	0.189	10.7
27R-2, 42-52	244.97	0.0976	1.78	16.6	0.193	6.1
30R-2, 140-150	274.95	0.0956	1.49	17.9	0.190	5.0
33R-1, 58-60	301.43	0.0952	2.42	13.6	0.194	7.8

Note: K_c = cell constant; R_s = sediment resistivity at measurement temperature (t); R_{pw} = pore water resistivity at 25°C; F = formation factor.

the alteration of volcanogenic material in the sediments as well as alteration reactions in the oceanic crust (e.g., Gieskes, 1983). Quantitatively, however, the changes are much more pronounced than usually observed. This is caused by the combined effect of abundant volcanogenic material, high formation factors, and rather high rates of sedimentation. The latter two factors render diffusive communication with the overlying seawater less efficient, thus allowing steeper concentration gradients to be maintained. The pronounced minimum of dissolved silica between 130 and 157 mbsf (Cores 126-787B-15R through -18R) indicates that silica is removed rapidly from the pore water in this region.

In contrast, below 140 mbsf the distribution of dissolved constituents is unusual. In deep-sea sediments the magnitude of the slopes of the various concentration profiles discussed above may vary vertically. However, except for sites with high bacterial activity, the slopes rarely change sign. At Site 787 the concentration profiles of potassium, magnesium, calcium, strontium, and

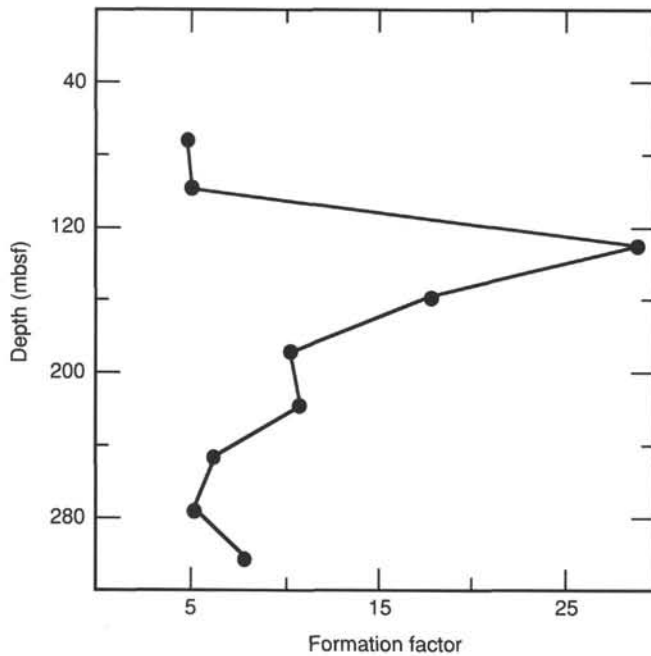


Figure 30. Formation factor of sediments from Hole 787B. The data are given in Table 6.

Table 7. Concentration of carbon and total nitrogen in sediments from Hole 787B.

Core, section, interval (cm)	Depth (mbsf)	Total carb. (%)	Inorg carb. (%)	Org carb. (%)	Total N (%)
126-787B-					
1R-1, 88.0-90.0	0.88	0.15	0.13	0.02	LD
2R-1, 80.0-82.0	3.10	0.33	0.28	0.05	0.01
2R-2, 120.0-122.0	5.00	0.15	0.15	LD	LD
2R-3, 47.0-49.0	5.77	1.84	1.30	0.54	0.06
3R-1, 56.0-58.0	12.46	1.44	1.35	0.09	0.01
3R-3, 29.0-31.0	15.19	0.20	0.17	0.03	LD
5R-1, 13.0-15.0	31.03	1.66	1.43	0.23	0.02
6R-1, 52.0-53.0	40.82	2.42	2.21	0.21	0.03
6R-2, 61.0-62.0	42.41	1.38	1.21	0.17	0.04
7R-1, 84.0-85.0	50.64	2.44	2.26	0.18	0.03
7R-2, 9.0-11.0	51.39	1.37	1.17	0.20	0.02
9R-1, 56.0-57.0	69.56	3.08	3.87	LD	0.03
9R-2, 34.0-35.0	70.84	1.28	0.92	0.36	0.03
9R-2, 65.0-75.0	71.15	4.28	4.09	0.19	0.03
9R-2, 65.0-75.0	71.15	4.52	4.15	0.37	0.03
9R-3, 33.0-34.0	71.58	0.99	0.86	0.13	0.04
10R-1, 64.0-66.0	79.34	0.57	0.34	0.23	0.04
11R-1, 27.0-29.0	88.67	7.96	7.73	0.23	0.03
11R-CC, 5.0-7.0	91.68	1.38	1.05	0.33	0.03
11R-CC, 5.0-7.0	91.68	1.20	1.05	0.15	0.04
12R-1, 3.0-13.0	98.13	4.35	4.14	0.21	0.05
12R-1, 3.0-13.0	98.13	4.91	4.75	0.16	0.02
12R-1, 88.0-90.0	98.98	2.78	2.66	0.12	0.03
12R-2, 63.0-65.0	100.23	6.31	6.19	0.12	0.01
14R-2, 12.0-14.0	119.12	0.32	0.34	0.00	LD
14R-3, 52.0-54.0	120.73	0.28	0.18	0.10	0.01
15R-1, 43.0-44.0	127.63	0.56	0.30	0.26	0.01
15R-2, 140.0-150.0	130.01	0.13	0.09	0.04	LD
18R-1, 80.0-90.0	157.00	0.15	0.12	0.03	LD
20R-1, 133.0-135.0	176.83	0.10	0.08	0.02	LD
20R-2, 32.0-34.0	180.32	0.19	0.13	0.06	0.01
21R-2, 140.0-150.0	188.00	2.69	2.49	0.20	0.01
24R-2, 140.0-150.0	217.00	1.69	1.68	0.01	0.01
27R-2, 42.0-52.0	244.92	1.48	1.43	0.05	0.01
30R-2, 140.0-150.0	274.90	0.47	0.37	0.10	LD
33R-1, 58.0-68.0	301.38	0.11	0.07	0.04	LD

Note: LD = less than detection limit.

sodium (Fig. 31) are reversed towards the bottom of the hole. DSDP Site 453, drilled in a sediment pond on the west side of the Mariana Trough, is one of the few Ocean Drilling Program (ODP)/DSDP sites showing this type of distribution pattern. Gieskes and Johnson (1982) reported concentration profiles of calcium, magnesium, strontium, potassium, lithium, and silica similar to the results obtained at Site 787. Their interpretation was that the pore water in the lower part of the sediment column is affected by the circulation of seawater through brecciated igneous and metamorphic rocks at the depth of maximum penetration. None of the explanations for the breccias suggested by the Leg 60 Shipboard Scientific Party (e.g., talus pile, avalanche deposits, drilling in a fault plane) could explain their character (Hussong, Uyeda, et al., 1982).

Because of insufficient penetration at Site 787, only a small portion of the lower part of the concentration profiles could be established. Therefore, the idea that the pore-water concentration profiles are shaped by circulating seawater will remain a vague hypothesis. On the basis of a rough extrapolation of the concentration profiles, the "aquifer" could be situated about 40-60 m below our maximum penetration of 320.1 mbsf. A less attractive interpretation of the concentration profiles involves progressive contamination of the pore water with the surface seawater with which we cleaned the bit. We took great care in choosing the part of the core to be squeezed, and only continuous, 10-cm-long, whole-round sections were sampled. The whole rounds were examined and the outer parts scraped off before squeezing. Unfortunately, there are no shipboard analyses that can be used to assess this question. Onshore analyses for one of the isotopes produced by nuclear testing (e.g., ³H, ⁹⁰Sr) or in nuclear reactors (e.g., ⁸⁵Kr) are needed.

Concentrations of sulfate and ammonia do not vary much, indicating that the bacterial activity in these low-organic-carbon sediments is minimal. This is further substantiated by the low levels of dissolved iron and manganese (Table 8). Evidently, the sub-bottom redox conditions are not sufficiently low enough to mobilize iron or manganese, except in the shallower intervals. The downhole decrease in alkalinity is probably caused by the precipitation of calcium carbonate in response to an increase in calcium from the alteration of volcanogenic material.

PHYSICAL PROPERTIES

Introduction

The techniques employed to acquire the physical property data at Site 787 are described in the "Explanatory Notes" chapter (this volume). Rotary drilling at this site resulted in significant disturbance to the unlithified sediment in Cores 126-787B-1R through -5R. Below Core 126-787B-5R, the recovered samples consisted of lithified or semilithified sediment (see "Lithostratigraphy and Accumulation Rates," this chapter). Consequently, no vane shear strength measurements were performed. Gamma-ray attenuation porosity evaluation (GRAPE) bulk-density measurements were run on most of the cores, but because the core sections did not completely fill the liners, the results are considered inaccurate (see the following discussion of index properties for more details).

Physical property measurements conducted on Hole 787B sediments include thermal conductivity, sonic (*P*-wave) velocity on discrete samples, wet-bulk density, porosity, water content, and grain density. Hole 787A, which consists of a single wash core, was not tested. Obviously spurious data are not recorded on the figures. However, all index property data are included in Table 9; anomalous data points are noted.

Index Properties

The results of all index property tests on Hole 787B sediments are presented in Table 9. Plots of the index property val-

Table 8. Composition of pore water from Site 787 sediments and of drilling-mud filtrate used during the drilling of Hole 787B.

Core, section, interval (cm)	Depth (mbsf)	pH	Alk. (mM)	Sal. (g/kg)	Cl ⁻ (mM)	SO ₄ ²⁻ (mM)	Na ⁺ (mM)	Mg ²⁺ (mM)	Ca ²⁺ (mM)	K (mM)	Li (μM)	Sr (μM)	Fe (μM)	Mn (μM)	SiO ₂ (μM)	NH ₄ ⁺ (μM)
126-787B-																
9R-2, 65-75	71.20	7.43	1.52	36.0	561	28.4	476	44.5	23.4	7.1	18.4	124	LD	51	843	100
12R-1, 3-13	98.18	7.16	1.09	35.0	542	27.6	444	37.9	35.3	3.9	16.9	151	12	95	559	69
15R-2, 146-156	130.21	ND	ND	ND	562	23.9	476	7.2	57.8	3.0	7.7	172	ND	ND	68	56
18R-1, 80-90	157.05	8.07	0.99	36.5	582	27.8	476	4.3	72.5	2.1	7.7	188	LD	9	94	60
21R-2, 140-150	187.95	8.54	0.62	37.5	572	25.5	465	1.3	79.0	1.9	9.2	180	LD	7	354	76
24R-2, 140-150	217.05	7.04	ND	38.0	590	26.3	467	3.5	79.8	2.0	7.7	170	LD	9	581	55
27R-2, 42-52	244.97	8.67	0.76	37.5	578	27.2	464	1.8	76.1	2.2	7.7	178	LD	9	485	47
30R-2, 140-150	274.95	8.55	0.37	38.0	586	29.7	480	2.6	76.6	2.7	7.7	195	LD	5	528	31
33R-1, 58-68	301.43	ND	ND	ND	575	30.7	488	15.5	55.1	4.2	12.3	163	LD	24	516	68
Drilling mud filtrate:		9.90	3.77	ND	25	5.0	30	2.9	0.3	1.4	15.8	2	LD	LD	132	11

Note: LD = less than detection; ND = not determined.

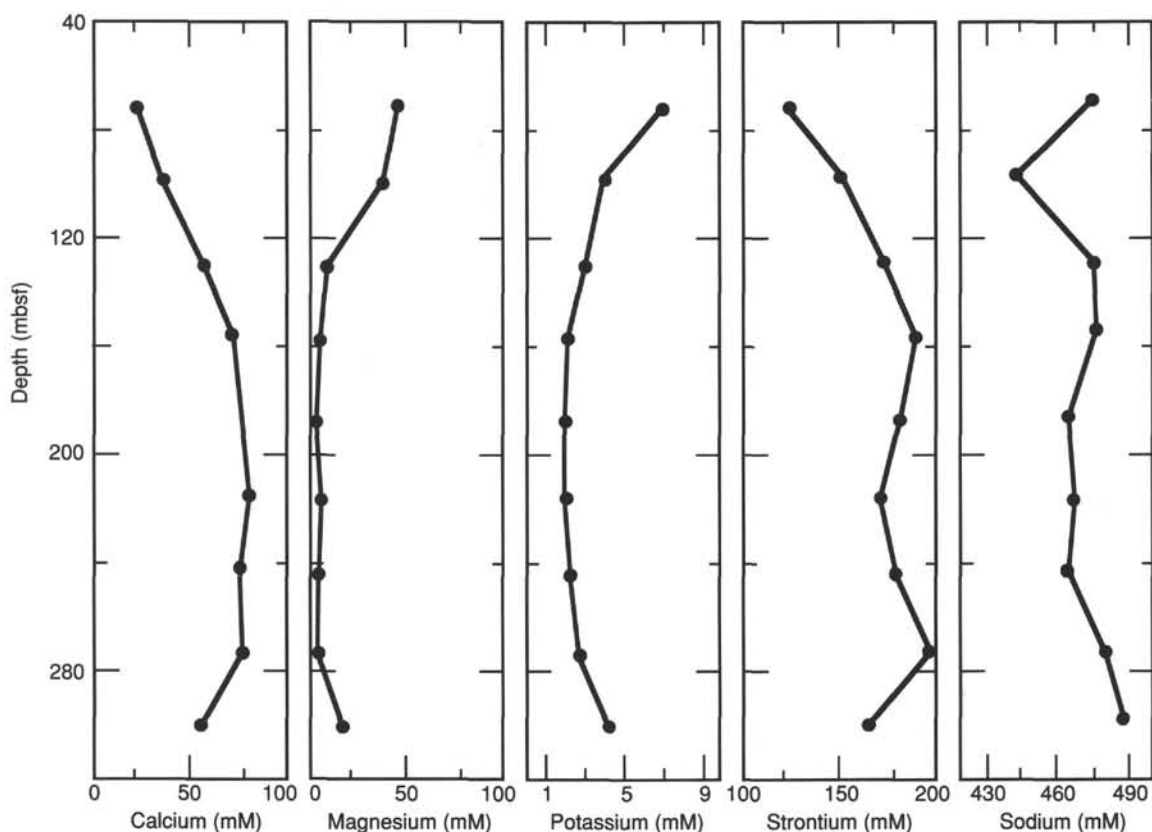


Figure 31. Composition of sediment pore waters, Hole 787B.

ues vs. sub-bottom depth in Hole 787B are presented in Figure 32.

The persistence of relatively high porosity values in deeper parts of the hole (e.g., as much as 60% at 280 mbsf, within the Oligocene sandstone unit) is surprising. Porosity values estimated from hand specimens and thin sections (see "Lithostratigraphy and Accumulation Rates," this chapter) of the recovered material are extremely low. Furthermore, applying Archie's Law (Archie, 1942), we calculated porosity values of approximately 20% and 30% for Samples 126-787B-13R-1, 56-58 cm, and -20R-1, 81-83 cm, respectively, from resistivity measurements. Index property measurements of these samples indicate porosities of 47% and 50%, respectively (Table 10).

There are several possible causes for these different porosity values. Archie's Law, which is empirically derived, may not be

appropriate for these samples. However, sampling with a water-cooled rock saw and/or uncertainties in the reliability of wet volumes determined by the pycnometer (Becker, Sakai, et al., 1988) also may bias the data (Table 11). In addition, porosity calculations using weights and dry volumes (Becker, Sakai, et al., 1988) are generally within 7% of the values obtained using the wet volumes. On the other hand, the porosity results obtained in Hole 787B are comparable to those previously reported for sediments from similar depositional/tectonic environments cored during ODP Leg 125 (Fryer, Pearce, Stokking, et al., in press) and DSDP Leg 60 (Hussong, Uyeda, et al., 1982).

Other explanations for the high porosity values include the presence of highly angular, porous volcanoclastic particles and an abundance of smectite minerals (see "Lithostratigraphy and

Table 9. Physical property data collected at Hole 787B.

Core, section, interval (cm)	Depth (mbsf)	Velocity (m/s)	Wet-bulk density (g/cm ³)	Grain density (g/cm ³)	Porosity (%)	Water content (%)	CaCO ₃ (%)	Thermal conductivity (W/m·K)
126-787B-								
1R-1, 34-35	0.34							^a 0.357
1R-1, 88-90	0.88		^a 2.11	^a 2.54	^a 37.8	^a 22.5	1.1	
2R-1, 43-45	2.73	4462						
2R-1, 88-82	3.18		^a 1.89	^a 2.67	^a 53.8	^a 40.6	2.3	
2R-2, 120-122	5.00		^a 1.99	^a 2.52	^a 44.5	^a 29	1.2	
2R-3, 47-49	5.77		^a 1.62	^a 2.53	^a 72.1	^a 83.9	10.8	
3R-1, 54-55	12.44							0.770
3R-1, 56-57	12.46		^a 1.7	^a 2.65	^a 65.6	^a 65.6	11.2	
3R-3, 28-29	15.18		^a 1.99	^a 1.85	^a 84.5	^a 77.3		
5R-1, 14-15	31.04		1.91	2.76	60.4	47.8	11.9	
6R-1, 52-54	40.82	1676	1.77	2.79	70.2	68.4	20.0	
6R-1, 102-103	41.32							^a 0.246
6R-2, 59-61	42.39	1667	1.72	2.71	70.4	72.0	10.1	^a 0.067
7R-1, 84-86	50.64	1765	1.74	2.82	60.1	54.7	18.8	
7R-1, 93-94	50.73							^a 0.728
7R-2, 9-11	51.39	1892	1.78	2.67	58.4	50.5	9.7	
8R-1, 24-26	59.54	1986	1.67	2.83	69.3	73.9		
8R-1, 37-38	59.67							^a 1.094
9R-1, 44-45	69.44							0.697
9R-1, 55-57	69.55	1680	^a 1.66	^a 2.79	^a 68.2	^a 72.5	32.2	
9R-2, 35-37	70.85	1708	1.80	2.87	63.6	56.5	7.7	
9R-3, 33-35	71.58	1836	1.93	2.77	67.3	55.7		
9R-3, 38-39	70.88							0.774
10R-1, 55-56	79.25							1.007
10R-1, 64-66	79.34	1825	1.68	2.77	65.5	66.8	3.3	
10R-2, 94-96	81.14	1841	1.87	2.82	56.3	44.6	60.0	
10R-3, 20-21	80.40							1.271
11R-1, 27-29	88.67	1886	1.92	2.67	51.7	38.2	64.4	
11R-1, 107-108	89.47							1.247
11R-2, 70-71	90.60							1.205
11R-CC, 5-7	91.68	1775	1.69	2.61	64.8	64.8	8.7	
12R-1, 3-13	98.13		2.04	2.86	52.5	35.9	22.2	
12R-1, 88-90	98.98	1671	1.94	2.74	53.4	39.4	39.6	
12R-1, 111-112	98.21							^a 1.532
12R-2, 48-49	100.08							1.234
12R-2, 63-65	100.23	1845	2.02	2.57	60.4	44.1	51.6	
13R-1, 56-58	108.36	3093	2.20	2.74	46.9	27.9		
13R-1, 64-68	108.44	3013	2.14	2.73	41.2	24.6		
13R-1, 94-96	108.74	3057	2.23	2.76	43.6	25.0		
13R-1, 111-113	108.91	3047	2.21	2.72	44.5	26.0		
13R-1, 123-136	109.03							1.190
13R-3, 115-117	111.25	1786	2.00	2.57	65.7	65.6	10.1	
13R-3, 119-120	111.99							1.003
14R-1, 115-117	118.65	2206	1.68	2.38	61.4	59.9	1.3	
14R-2, 12-14	119.12	2610	1.96	2.49	46.5	32.2	2.8	
14R-3, 52-54	120.73	2872	2.05	2.60	44.2	28.4	1.5	
15R-1, 72-74	127.92	2773	2.05	2.54	46.5	30.3	2.5	
15R-3, 29-31	130.44	2773	2.17	2.71	45.5	27.4	0.8	
15R-4, 89-90	220.70							0.970
15R-4, 92-94	132.57	2206	1.72	2.54	65.9	64.6	0.8	
16R-1, 138-140	138.18	1960	1.83	2.64	60.7	51.4	11.3	
16R-2, 90-91	139.20							1.081
16R-2, 125-127	139.55	1942	1.89	2.71	58.8	46.7	8.7	
16R-3, 72-73	140.52							0.929
16R-4, 103-105	142.33	1980	1.82	2.58	58.8	49.4	21.9	
16R-CC, 17-19	142.97	2210	1.92	2.55	58.7	45.7	0.9	
17R-1, 75-77	147.25	1945	^a 1.92	^a 3.01	^a 36.0	^a 23.7	8.6	
17R-1, 80-81	147.31							1.102
17R-2, 123-125	149.23	2220	1.98	2.74	60.8	45.9	1.0	
17R-3, 66-68	150.16	2340	2.08	2.97	61.7	43.7	0.7	
17R-5, 20-21	152.70							^a 1.140
17R-5, 74-76	153.24	1969	1.85	2.47	53.5	42.2	6.1	
18R-1, 46-48	156.66	2055	1.94	2.51	46.3	32.3	1.8	
18R-1, 80-90	157.00		2.07	2.52	43.1	27.0		
18R-2, 10-11	157.80							^a 1.190
18R-3, 118-120	159.78	1924	1.90	2.62	54.1	41.3	1.0	
19R-2, 38-40	167.68	2186	1.99	2.76	61.7	46.5	1.8	
19R-4, 46-48	170.76	1952	2.06	3.01	55.8	38.3	10.5	
19R-6, 52-54	173.82	2235	2.11	2.83	54.6	36.0	0.7	
20R-1, 81-83	176.31	2433	2.13	2.81	52.2	33.5	0.7	
20R-1, 133-135	176.83	2516	2.07	2.71	48.1	31.2	0.8	
20R-2, 7-9	177.07	2628	2.07	2.74	49.9	32.7		
20R-2, 57-60	177.57	2257	1.94	2.79	59.3	45.8		
20R-4, 32-34	180.32	2168	2.10	2.77	45.8	28.7	1.1	
21R-1, 52-54	185.62	2498	2.23	2.94	41.8	23.7	0.7	

Table 9 (continued).

Core, section, interval (cm)	Depth (mbsf)	Velocity (m/s)	Wet-bulk density (g/cm ³)	Grain density (g/cm ³)	Porosity (%)	Water content (%)	CaCO ₃ (%)	Thermal conductivity (W/m·K)
126-787B-								
21R-2, 140-150	188.00		2.12	2.55	49.4	31.3		
21R-3, 65-67	188.75	2033	2.05	2.80	50.8	34.1	20.7	
21R-4, 35-37	189.95	2251	2.05	2.75	50.4	33.6	0.7	
21R-5, 100-102	192.10	2212	2.03	2.83	51.6	35.2	1.7	
21R-6, 93-95	193.53	1964	1.97	2.75	51.8	36.9	15.0	
22R-1, 75-77	195.55	2490	2.21	2.75	39.2	22.3		
23R-2, 52-54	206.42	2237	1.96	2.67	51.0	36.4	8.9	
23R-4, 63-65	209.53	2565	2.31	2.88	36.7	19.4	0.7	
23R-5, 77-79	211.17	3130	2.40	2.81	37.2	18.9	1.7	
24R-1, 110-112	215.20	2442	2.11	2.70	46.8	29.5	0.8	
24R-2, 140-150	217.00		1.84	2.44	57.0	46.7	11.0	
24R-3, 29-31	217.39	2095	2.07	2.68	53.9	36.5	14.0	
24R-4, 77-79	219.37	2266	1.95	2.49	48.2	33.9		
24R-5, 97-99	221.07	2161	1.76	2.42	55.9	48.2	0.2	
24R-6, 25-27	221.85	2355	1.84	2.51	58.5	48.4	10.4	
24R-7, 58-60	223.08	2537	2.14	2.90	50.5	31.9	60.0	
25R-1, 53-55	224.23	2139	1.74	2.49	61.5	56.8	15.3	
25R-1, 67-69	224.37	2043	1.74	2.49	61.5	57.0	4.8	
25R-1, 84-86	224.54	2034	1.74	2.37	57.0	50.4	0.9	
25R-1, 95-97	224.65	2069	1.79	2.32	58.0	49.8	0.3	
25R-1, 117-119	224.87	2113	1.79	^a 2.99	^a 38.6	^a 28.4	0.5	
25R-4, 117-119	229.37	2252	2.08	2.66	47.2	30.3	35.8	
25R-6, 4-6	231.24	2531	2.27	2.79	51.6	30.4	0.8	
26R-1, 82-84	234.22	2173	2.06	2.73	46.1	29.8	18.7	
26R-3, 86-88	237.26	2130	1.74	2.73	66.8	64.5		
26R-4, 145-147	239.35	2292					1.4	
26R-5, 47-49	239.87	2304	1.75	2.63	63.2	58.8	6.2	
27R-1, 122-124	244.22	2075	2.02	2.84	52.4	36.2	10.7	
27R-2, 42-52	244.92		2.01	2.83	51.0	35.1		
27R-2, 122-124	245.72	2432	1.97	2.75	59.0	44.8	11.9	
27R-4, 81-83	247.58	1987	1.87	2.80	59.7	48.6	25.1	
27R-CC, 11-13	248.24	3483	2.22	2.92	45.1	26.2	1.8	
28R-1, 45-47	253.15	2695	2.15	2.91	47.2	28.9	1.2	
28R-2, 146-148	255.66	2243	1.93	2.82	58.3	44.8	18.2	
28R-4, 93-95	258.13	2416	^a 2.33	^a 2.76	^a 35.3	^a 18.4	41.3	
28R-5, 122-124	259.77	2039	1.96	2.85	60.0	45.5	39.7	
29R-1, 95-97	263.35	2336	^a 2.28	^a 2.82	^a 35.4	^a 18.9	43.3	
29R-2, 70-72	264.60	1991	1.82	2.67	59.1	49.7	1.7	
29R-3, 69-71	266.09	2140	1.89	2.81	60.9	49.4	16.4	
29R-4, 43-45	267.33	1856	1.73	2.59	62.3	58.2		
29R-5, 107-109	269.47	2166	1.86	2.85	61.0	50.4	17.2	
30R-1, 104-106	273.04	2069	1.79	2.85	65.3	59.5	26.8	
30R-2, 140-150	274.90		1.79	2.57	59.9	52.2	3.1	
30R-3, 60-62	275.60	1991	1.94	2.57	58.9	45.1	0.9	
30R-4, 55-57	277.05	1993	1.88	2.78	58.4	46.8	23.7	
30R-5, 75-77	278.75	2090	1.87	2.83	63.1	52.7	35.7	
31R-1, 112-114	282.82	2899	2.28	2.94	41.8	23.2	26.8	
32R-1, 122-124	292.52	2850	2.31	2.89	44.4	24.5	0.9	
32R-2, 81-83	293.61	2660	2.07	2.72	51.9	34.5	8.2	
33R-1, 58-68	301.38		2.29	2.94	38.2	20.5	0.6	
33R-2, 61-63	302.09	2690	2.13	2.84	47.3	29.5	0.6	
34R-1, 50-52	311.00	2246	2.00	2.95	55.1	39.2		

^a Indicates a value that is obviously spurious and has not been plotted in Figures 33, 34, 36, or 37.

Accumulation Rates," this chapter). Angular particles will result in a less densely packed, higher porosity sediment; smectite is associated with high porosity and water content because of its small size, high specific surface area, and propensity for adsorption of water (e.g., see discussion by Mitchell, 1976). Nevertheless, we recommend that the index property data be considered primarily as trends, rather than as absolute values.

GRAPE wet-bulk density measurements were conducted on Cores 126-787B-3R through -13R. However, rotary drilling caused reduction of core diameters, resulting in gaps between the core and liner. Because the GRAPE technique requires that the sediment completely fill the liners (Boyce, 1976), the GRAPE measurements are probably incorrect. A comparison of GRAPE and gravimetric bulk-density values for the depth interval between Sections 126-787B-9R-1 and -9R-3 (Fig. 33) supports this

hypothesis. All GRAPE data fall below the gravimetrically determined values.

Porosity and water content values decrease downhole and are overprinted by significant small-scale variability. Much of the variability of the index properties, particularly in Subunit IVA, may be attributed to the existence of turbidite beds. Because our sampling scheme included representative samples from all turbidite lithologies, the high variability in the properties is not surprising. A detailed investigation of one turbidite sequence showed that physical properties change dramatically over short depth intervals within a single turbidite bed (Fig. 34).

An exception to the trend of decreasing porosity and water content with depth is found in Unit I, where these parameters actually increase with depth (Fig. 32). Sediments in this unit consist primarily of unlithified sand and are strongly disturbed

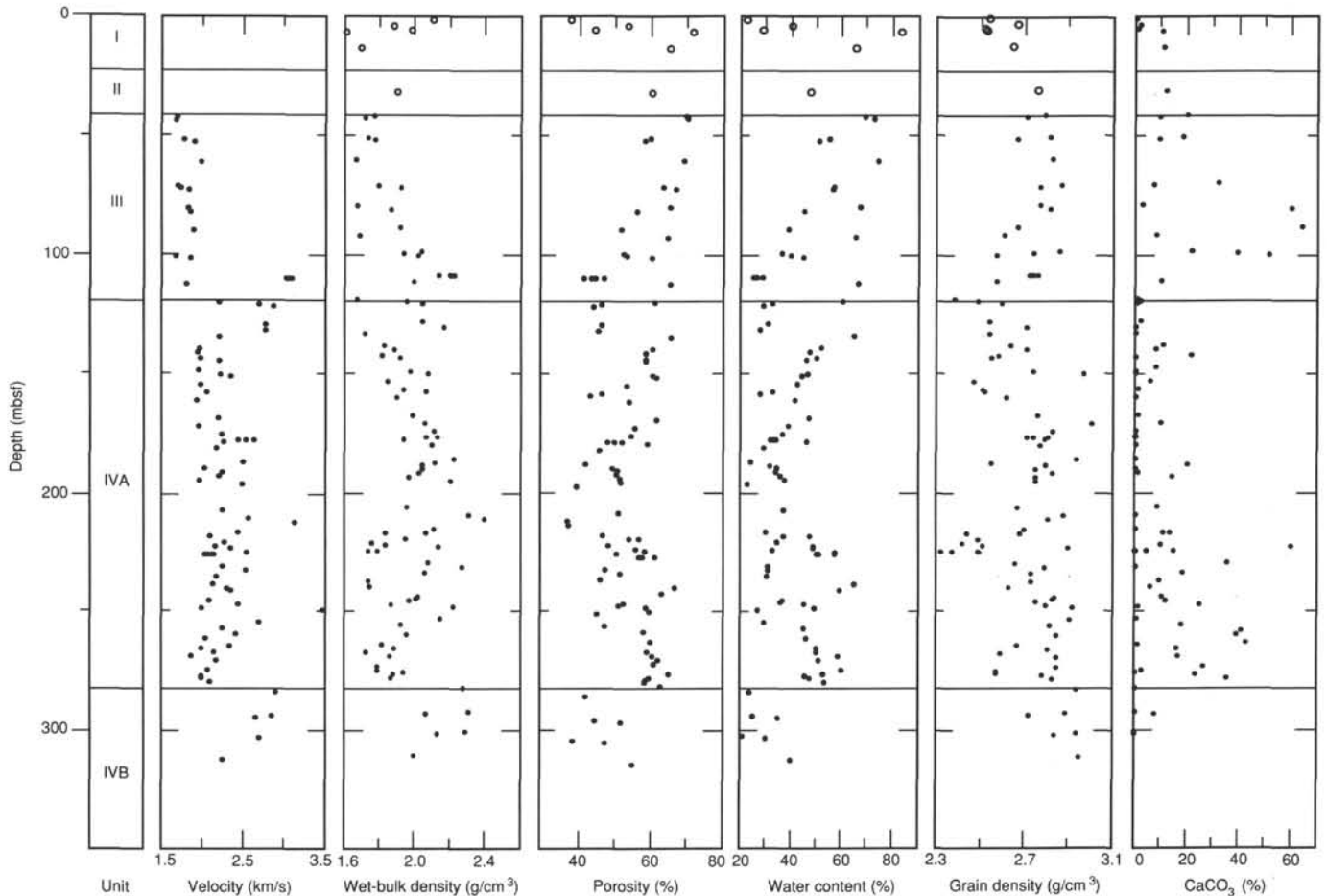


Figure 32. Physical properties plotted vs. depth (mbsf) and lithostratigraphic unit, Hole 787B. Open circles represent suspect data measured on unlithified (Unit I) and poorly lithified (Unit II) sediments.

Table 10. Comparison of porosity derived from index-property data and resistivity (using Archie's Law), Hole 787B.

Core, section, interval (cm)	Depth (mbsf)	Resistivity (ohm-m)	Porosity (from resistivity) (%)	Porosity (from index properties) (%)
126-787B-				
13R-1, 56-58	108.36	4.79	20	47
13R-1, 94-96	108.74	5.56	19	44
13R-1, 111-113	108.91	5.31	19	45
20R-2, 6-8	177.07	2.55	28	50
20R-2, 57-59	177.57	1.69	34	59
20R-1, 81-83	176.31	1.74	34	52

by drilling. The anomalous increases in porosity and water content are probably the result of sample contamination by drilling fluid.

Contacts between the four lithologic units are clearly visible in the index property data. Distinct changes in porosity, bulk density, and water content are observed at these depths (Fig. 32). In addition, porosity and bulk-density data display slightly different trends within the different units. The lapilli tuff reported at the base of Unit III (see "Lithostratigraphy and Accumulation Rates," this chapter) is delineated in the index property values by low porosities and high bulk-density values.

Calcium carbonate content is relatively high in the upper three lithologic units (Fig. 32), with a maximum of 65% at 89 mbsf (Section 126-787B-11R-1); it is consistent with the occur-

rence of nanofossil chalks and nanofossil-rich claystones that constitute those units ("Lithostratigraphy and Accumulation Rates," this chapter). Calcium carbonate values decrease at the Unit III/IV boundary, as does the bulk density. Carbonate contents average about 4% from 120 to 180 mbsf (Sections 126-787B-14R-2 to -20R-4). The mean carbonate value increases below 180 mbsf to 14.5%, but variability also increases. Values decrease similarly near the bottom of the hole (Subunit IVB). Because carbonate dissolution is minimal at this site (see "Biostratigraphy," this chapter), the lower CaCO₃ contents probably result from dilution brought about by the increased influx of volcanoclastic material in the form of turbidites and other gravity-controlled sedimentary flows. The influence of turbidites on CaCO₃ content is shown in Figure 34. Within this single turbidite bed, low CaCO₃ contents are observed in the coarse lower parts and higher CaCO₃ contents in the upper hemipelagic division. Variations in carbonate content also are influenced by our sampling scheme, which included single samples from numerous different turbidite layers (see discussion above and Fig. 34).

We observed a positive relationship between grain density and bulk density, and an inverse correlation between wet-bulk density and porosity at this site. These relationships have been observed elsewhere in Pacific sediments (e.g., Wilkens and Handyside, 1983). However, bulk-density values from Hole 787B tend to be greater than expected, compared to calculated relationships for constant grain density (Wilkens and Handyside, 1983). Again, the possibility of inaccurate porosity values may explain some of this discrepancy.

Table 11.
Calibration
measurements
for the penta-
pycnometer,
Hole 787B.

Run no.	Volume (cm ³)
1	16.3205
2	16.3227
3	16.3352
4	16.3242
5	16.3337
6	16.3456
7	16.3538
8	16.3534
9	16.3410
10	16.3694
11	16.3524
12	16.3359
13	16.3540
14	16.3518
15	16.3504
16	16.3457
17	16.3303
18	16.3469
19	16.3446
20	16.3401
21	16.3395
22	16.3382
23	16.3470
24	16.3440
25	16.3491

Note: standard known volume = 16.38 cm³; mean value = 16.3428; standard deviation = ±0.0112.

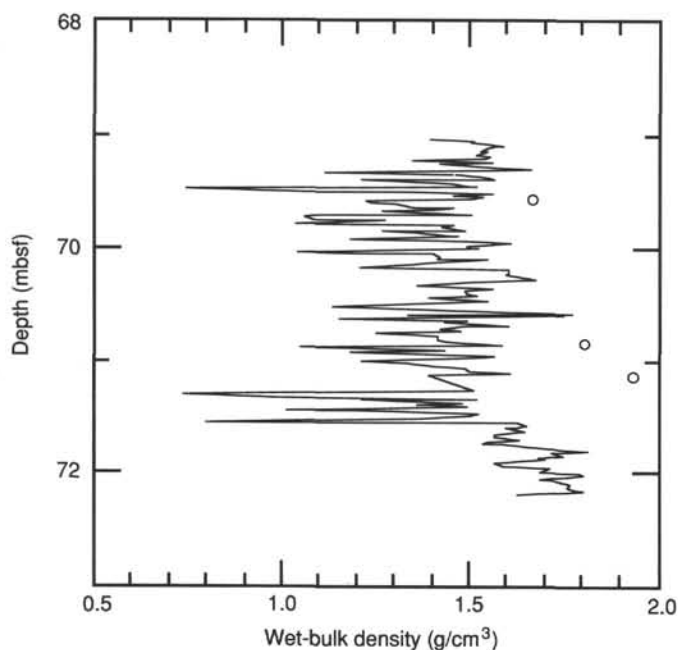


Figure 33. Plot of wet-bulk density determined gravimetrically (open circles) and by GRAPE (solid line) for Core 126-787B-9R.

Sonic Velocity

Sonic velocity measurements were performed on discrete samples from Site 787 cores (Tables 9 and 12; Figs. 32, 34, and 35). Because of the reduced core diameters that were a result of the rotary drilling, multisensor track (MST) sonic velocities were not measured. Coarse, unconsolidated sediments at the top of the hole also prevented Hamilton Frame velocity analyses on Cores 126-787B-1R through -4R. We observed a general increase in sonic velocity with depth. Unit III is characterized by relative uniform velocities ranging from 1.67 to 3.1 km/s. Above the lapilli tuff in Unit III, velocities average 1.71 km/s. Velocities from four samples within the lapilli tuff are 3.0–3.1 km/s, whereas below this tuff, velocities drop to 1.79 km/s within a fine-grained sedimentary unit.

At the top of Subunit IVA, velocities range from 2.21 to 2.87 km/s within a coarse, consolidated sand unit. Velocities within Subunit IVA range from 1.92 to 3.50 km/s and average 2.26 km/s. This unit is characterized by high-frequency fluctuations in velocity that may be attributed to the abundance of turbidite beds and other sedimentary structures indicative of downslope processes. As we usually performed the velocity measurements on one sample per section, we took representative samples from various levels within turbidite beds from section to section, but not within a single turbidite. This may explain the high-frequency scatter observed in the data shown in Figure 32. To illustrate this point, the results of a detailed study of a single turbidite sequence from Core 126-787B-25R-1 are shown in Figure 34. In this core, the physical property measurements exhibit significant changes, including a velocity variation of over 100 m/s. This study exemplifies the problem of sampling only once per section in areas of rapidly changing, thinly bedded lithologies. Subunit IVB, a pebbly sandstone, is characterized by velocities that range from 2.25 to 2.90 km/s and average 2.67 km/s.

Thermal Conductivity

All thermal conductivity results are presented in Table 9. Only values that fall within acceptable temperature drift rates (<0.04°C/min) and curve fit parameters (<0.015) are shown in Figure 36. Thermal conductivity measurements range from 0.697 to 1.271 W/m · K. Values measured above 75 mbsf are distinctly lower (average = ~0.75 W/m · K) than those below (average = ~1.11 W/m · K). Higher thermal conductivity values below 75 mbsf correlate with increased wet-bulk density and decreased porosity.

REFERENCES

- Archie, G., 1942. The electrical resistivity log as an aid in determining some reservoir characteristics. *AIME Trans.*, 146:54.
- Arthur, M. A., Carson, B., and von Huene, R., 1980. Initial tectonic deformation of hemipelagic sediment at the leading edge of the Japan convergent margin. In Langseth, M., Okada, H., et al., *Init. Repts. DSDP*, 56, 57, Pt. 1: Washington (U.S. Govt. Printing Office), 569–613.
- Becker, K., Sakai, H., et al., 1988. *Proc. ODP, Init. Repts.*, 111: College Station, TX (Ocean Drilling Program).
- Berggren, W. A., Kent, D. V., Flynn, J. J., and Van Couvering, J. A., 1985. Cenozoic geochronology. *Geol. Soc. Am. Bull.*, 96:1407–1418.
- Bouma, A. H., 1962. *Sedimentology of Some Flysch Deposits*: Amsterdam (Elsevier).
- Boyce, R., 1976. Definitions and laboratory techniques of compressional sound velocity parameters and wet-water content, wet-bulk density, and porosity parameters by gravimetric and gamma-ray attenuation techniques. In Schlanger, S., Jackson, E., et al., *Init. Repts. DSDP*, 33: Washington (U.S. Govt. Printing Office), 695–728.
- Fryer, P., Langmuir, C. H., Taylor, B., Zhang, Y., and Hussong, D. M., 1985. Rifting of the Izu Arc, III. Relationship of chemistry to tectonics. *Eos*, 66(18):421.
- Fryer, P., Pearce, J., Stokking, L. B., et al., in press. *Proc. ODP, Init. Repts.*, 125: College Station, TX (Ocean Drilling Program).

- Gieskes, J. M., 1983. The chemistry of interstitial waters of deep-sea sediments: interpretation of deep sea drilling data. In Riley, J. P., and Chester, R. (Eds.), *Chemical Oceanography* (Vol. 8): London (Academic Press), 221-269.
- Gieskes, J. M., and Johnson, J., 1982. Interstitial water studies, Deep Sea Drilling Project Leg 60. In Hussong, D. M., Uyeda, S., et al., *Init. Repts. DSDP, 60*: Washington (U.S. Govt. Printing Office), 749-754.
- Hussong, D. M., and Uyeda, S., 1982. Tectonic processes and the history of the Mariana Arc: a synthesis of the results of Deep Sea Drilling Project Leg 60. In Hussong, D. M., Uyeda, S., et al., *Init. Repts. DSDP, 60*: Washington (U.S. Govt. Printing Office), 909-929.
- Hussong, D., Uyeda, S., et al., 1982. *Init. Repts. DSDP, 60*: Washington (U.S. Govt. Printing Office).
- Kaiho, K., in press. Morphotype changes of deep-sea benthic foraminifera during the Cenozoic Era and their paleoenvironmental implications. *Kaseki* (Fossils).
- Kastner, M., 1979. Zeolites. *Reviews in Mineralogy*, 6:111-122.
- Kinoshita, H., 1980. Paleomagnetism of sediment cores from Deep Sea Drilling Project Leg 58, Philippine Sea. In Klein, G. deV., Kobayashi, K., et al., *Init. Repts. DSDP, 58*: Washington (U.S. Govt. Printing Office), 765-768.
- Klaus, A., and Taylor, B., in press. Submarine canyon development in the Izu-Bonin forearc: a SeaMARC II survey of Aoga Shima canyon. *GSA Bull.*
- Louden, K. E., 1977. Paleomagnetism of DSDP sediments, phase shifting of magnetic anomalies, and rotations of the West Philippine Basin. *J. Geophys. Res.*, 82:2989-3002.
- Lundberg, N., and Leggett, J. K., 1986. Structural features in cores from the slope landward of the Japan Trench, Deep Sea Drilling Project Leg 87B. In Kagami, H., Karig, D. E., Coulbourn, W. T., et al., *Init. Repts. DSDP, 87*: Washington (U.S. Govt. Printing Office), 807-842.
- Mitchell, J., 1976. *Fundamentals of Soil Behavior*: New York (Wiley and Sons).
- Nilsen, T. H., and Abbott, P. L., 1981. Paleogeography and sedimentology of Upper Cretaceous turbidites, San Diego, California. *AAPG Bull.*, 5:1256-1284.
- Ogawa, Y., and Miyata, Y., 1985. Vein structure and its deformation history in the sedimentary rocks of the Middle America Trench slope off Guatemala, Deep Sea Drilling Project Leg 84. In von Huene, R., Aubouin, J., et al., *Init. Repts. DSDP, 84*: Washington (U.S. Govt. Printing Office), 811-829.
- Okada, H., and Bukry, D., 1980. Supplementary modification and introduction of code numbers to the low-latitude coccolith biostratigraphic zonation. *Mar. Micropaleontol.*, 5:321-325.
- Pickering, K. T., Hiscott, R. N., and Hein, F. J., 1989. *Deep Marine Environments: Clastic Sedimentation and Tectonics*: London (Unwin Hyman).
- Ricci Lucchi, F., and Valmori, E., 1980. Basin-wide turbidites in a Miocene, over-supplied deep-sea plain: a geometrical analysis. *Sedimentology*, 27:241-270.
- Stow, D.A.V., Howell, D. G., and Nelson, C. H., 1985. Sedimentary, tectonic, and sea-level controls. In Bouma, A. H., Normark, W. R., and Barnes, N. E. (Eds.), *Submarine Fans and Related Turbidite Systems*: Berlin-Heidelberg-New York (Springer-Verlag), 15-22.
- Wilkins, R., and Handyside, T., 1983. Physical properties of equatorial Pacific sediments. In Mayer, L., Theyer, F., et al., *Init. Repts. DSDP, 85*: Washington (U.S. Govt. Printing Office), 839-847.

Ms 126A-106

NOTE: All core description forms ("barrel sheets") and core photographs have been printed on coated paper and bound as Section 3, near the back of the book, beginning on page 421.

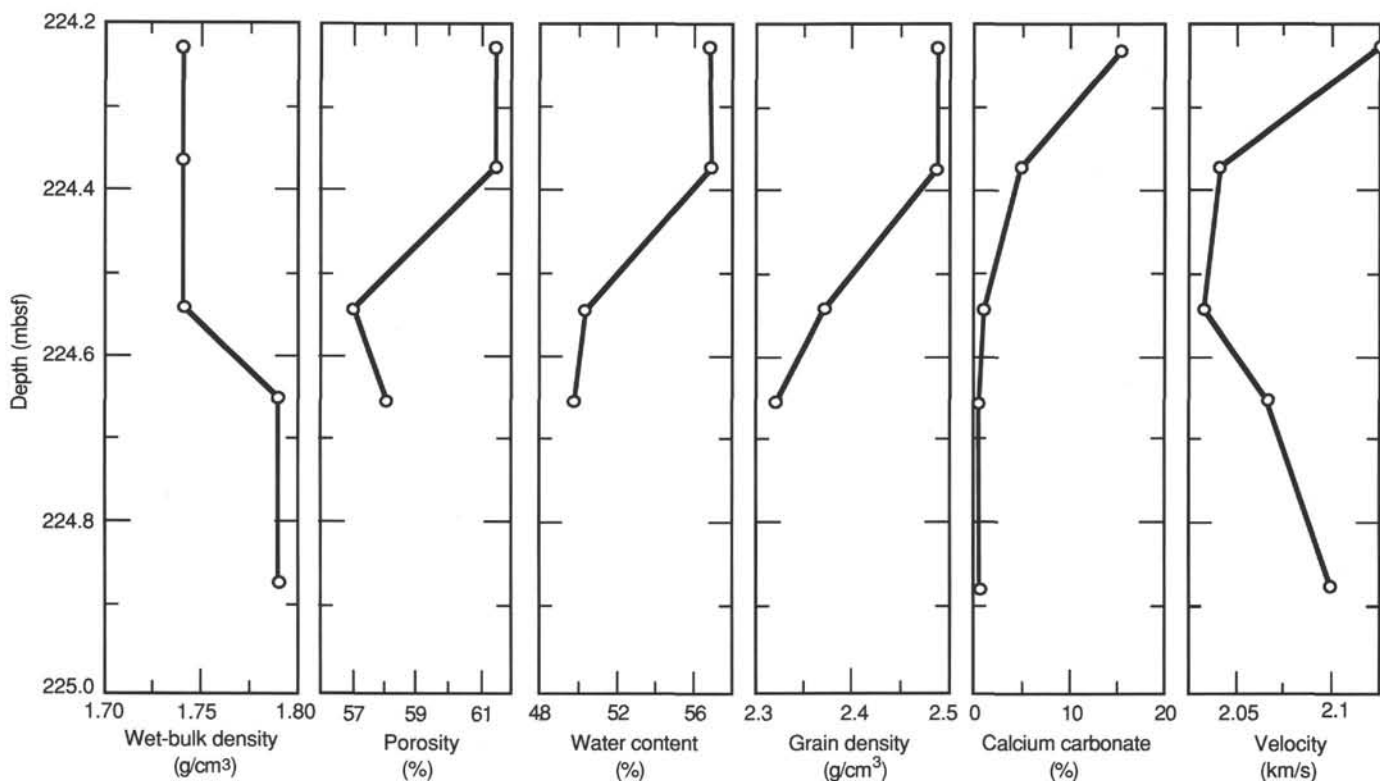


Figure 34. Physical properties plotted vs. depth for five samples from a single turbidite bed within Subunit IVA, including (from bottom to top): the lower coarse part of the basal parallel-laminated sand division, the upper fine part of the basal parallel-laminated sand division, the cross-laminated T_c division, the finely-laminated T_d division, and a bioturbated hemipelagic unit.

Table 12. Results of Hamilton Frame calibration using lucite and aluminum standards of varying length.

	Thickness (mm)	Traveltime (μs)
Cores 126-787B-1R to -20R		
Lucite	10.00	4.69
	20.10	8.46
	40.10	15.97
	50.19	19.68
	65.70	25.55
$t = 0.941 + 0.347x$ for $x = 0, t = 0.941 \mu s$		
Aluminum	20.00	4.10
	30.00	5.62
	40.00	7.16
	50.00	8.70
	$t = 1.026 + 0.153x$ for $x = 0, t = 1.026 \mu s$; Average delay time = 0.984 μs	
Cores 126-787B-21R to -34R		
Lucite	9.70	4.66
	19.75	8.39
	39.75	15.90
	49.90	19.66
	65.55	25.51
$t = 1.033 + 0.374x$ for $x = 0, t = 1.033 \mu s$		
Aluminum	19.90	4.03
	29.90	5.52
	40.00	7.07
	50.00	8.60
	$t = 0.993 + 0.152x$ for $x = 0, t = 0.993 \mu s$; Average delay time = 1.013 μs	

Note: data are plotted in Figure 35.

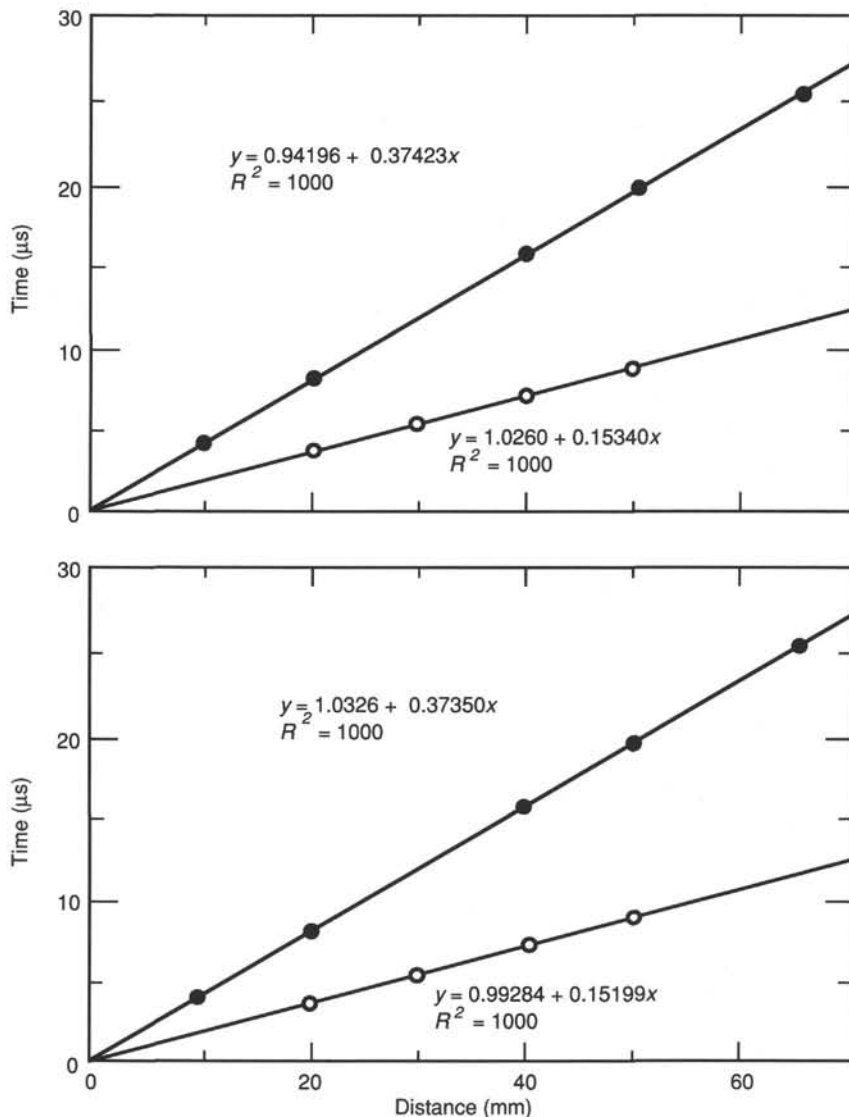


Figure 35. Plots of Hamilton Frame velocimeter calibrations showing the results from lucite (solid circles) and aluminum (open circles) standards. **A.** Cores 126-787B-1R through -20R. **B.** Cores 126-787B-21R through -34R.

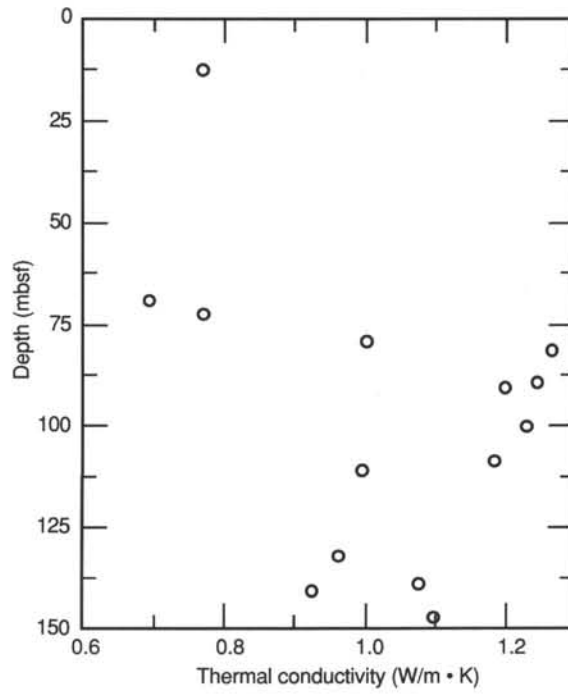


Figure 36. Thermal conductivity vs. depth, Hole 787B.